

Supporting Information for:

# Cu Intercalation and Defect Engineering Realize Atomic-Scale Hydrogen Spillover Effect in NbS<sub>2</sub> to Boost Acidic Hydrogen Evolution

Haoyu Yue, Zhongnan Guo,<sup>\*</sup> Jiaqi Fan, Pu Wang, Shuang Zhen, and Wenxia Yuan,<sup>\*</sup>

Department of Chemistry, School of Chemistry and Biological Engineering, University of Science and  
Technology Beijing, Beijing, 100083, China

# CONTENTS

## Experimental details

**Fig. S1** Schematic diagram of the synthesis process of  $\text{Cu}_{0.4}\text{NbS}_2$  and  $\text{Cu}_{0.4}\text{NbS}_{2-\delta}$  polycrystalline samples.

**Fig. S2** The XRD patterns of  $\text{Cu}_x\text{NbS}_2$  ( $x = 0, 0.05, 0.1, 0.2, 0.3, 0.4, 0.5, 0.65, 0.7$  and  $0.8$ ). The right part shows the enlarged (002)/(003) diffraction peaks of the samples.

**Fig. S3** Rietveld refinement of the PXRD pattern of  $\text{Cu}_{0.1}\text{NbS}_2$ .

**Fig. S4** Rietveld refinement of the PXRD pattern of  $\text{Cu}_{0.4}\text{NbS}_2$ .

**Fig. S5** The XRD patterns of  $\text{Cu}_{0.4}\text{NbS}_{2-\delta}$  with different mass ratios of  $\text{Cu}_{0.4}\text{NbS}_2 : \text{NaBH}_4 = 1:1, 1:3$  and  $1:5$ .

**Fig. S6** Raman spectra of  $3\text{R-NbS}_2, \text{Cu}_{0.1}\text{NbS}_2$  and  $\text{Cu}_{0.4}\text{NbS}_2$ . The spectra of  $3\text{R-NbS}_2$  and  $\text{Cu}_{0.4}\text{NbS}_2$  were also used in the main text in Fig. 1d.

**Fig. S7** Full XPS spectra of  $3\text{R-NbS}_2, \text{Cu}_{0.4}\text{NbS}_2$  and  $\text{Cu}_{0.4}\text{NbS}_{2-\delta}$ .

**Fig. S8** The SEM images of (a)  $\text{NbS}_2$  and (b)  $\text{Cu}_{0.4}\text{NbS}_2$ .

**Fig. S9** The SEM images of  $\text{Cu}_{0.4}\text{NbS}_2$  (a) before and (b) after SPR.

**Fig. S10** (a) The SEM image and the elemental mapping of  $\text{NbS}_2$ ; (b) The EDS results of  $\text{NbS}_2$ ; (c) the SEM image and the elemental mapping of  $\text{Cu}_{0.4}\text{NbS}_2$ ; (d) The EDS results of  $\text{Cu}_{0.4}\text{NbS}_2$ .

**Fig. S11** (a) The TEM image of  $\text{Cu}_{0.4}\text{NbS}_2$ ; (b) The corresponding SAED pattern; (c) The HRTEM images of  $\text{Cu}_{0.4}\text{NbS}_2$ .

**Fig. S12** HER polarization curves of the  $\text{Cu}_x\text{NbS}_2$  ( $x = 0, 0.05, 0.1, 0.2, 0.3, 0.4, 0.5$  and  $0.65$ ).

**Fig. S13** HER polarization curves of  $\text{Cu}_{0.4}\text{NbS}_{2-\delta}$  with different mass ratios of  $\text{Cu}_{0.4}\text{NbS}_2 : \text{NaBH}_4 = 1:1, 1:3$  and  $1:5$ .

**Fig. S14** CV curves measured at different scan rates of (a)  $\text{NbS}_2$ , (b)  $\text{Cu}_{0.4}\text{NbS}_2$ , and (c)  $\text{Cu}_{0.4}\text{NbS}_{2-\delta}$ .

**Fig. S15** Nyquist plot for (a)  $\text{Cu}_{0.4}\text{NbS}_2$  and (b)  $\text{Cu}_{0.4}\text{NbS}_{2-\delta}$  catalyst at various HER overpotentials (The inset is the equivalent circuit for the simulation); (c) EIS-derived Tafel plots of the  $\text{Cu}_{0.4}\text{NbS}_2$  and (b)  $\text{Cu}_{0.4}\text{NbS}_{2-\delta}$  catalysts obtained from the hydrogen adsorption resistance  $R_2$ .

**Fig. S16** (a) Turnover frequency (TOF) of NbS<sub>2</sub>, Cu<sub>0.4</sub>NbS<sub>2</sub> and Cu<sub>0.4</sub>NbS<sub>2-δ</sub>; (b) TOF of NbS<sub>2</sub>, Cu<sub>0.4</sub>NbS<sub>2</sub> and Cu<sub>0.4</sub>NbS<sub>2-δ</sub> at an overpotential of 300 mV for the HER.

**Fig. S17** Faradaic efficiency of H<sub>2</sub> production upon operation time.

**Fig. S18** The XRD patterns of Cu<sub>0.4</sub>NbS<sub>2-δ</sub> before and after 3000th cycles.

**Fig. S19** Raman spectra of Cu<sub>0.4</sub>NbS<sub>2-δ</sub> before and after 3000th cycles.

**Fig. S20** EPR spectra of Cu<sub>0.4</sub>NbS<sub>2-δ</sub> before and after 3000th cycles.

**Fig. S21** High resolution XPS spectra of (a) Nb 3d, (b) S 2p and (c) Cu 2p in Cu<sub>0.4</sub>NbS<sub>2-δ</sub> before and after 3000th cycles.

**Fig. S22** The SEM image of Cu<sub>0.4</sub>NbS<sub>2-δ</sub> after 3000th cycles.

**Fig. S23** The TEM images of Cu<sub>0.4</sub>NbS<sub>2-δ</sub> after 3000th cycles.

**Fig. S24** The single layer models of NbS<sub>2</sub>, Cu<sub>0.1</sub>NbS<sub>2</sub>, Cu<sub>0.4</sub>NbS<sub>2</sub> and Cu<sub>0.4</sub>NbS<sub>2-δ</sub> for calculation.

**Fig. S25** The Bader charge of different Nb and Cu sites in Cu<sub>0.4</sub>NbS<sub>2-δ</sub> after the S vacancy induced.

**Fig. S26** Partial charge density of NbS<sub>2</sub>, Cu<sub>0.1</sub>NbS<sub>2</sub>, Cu<sub>0.4</sub>NbS<sub>2</sub> and Cu<sub>0.4</sub>NbS<sub>2-δ</sub> within 1.0 eV below fermi level.

**Fig. S27** The band structures of (a) NbS<sub>2</sub>, (b) Cu<sub>0.1</sub>NbS<sub>2</sub>, (c) Cu<sub>0.4</sub>NbS<sub>2</sub> and (d) Cu<sub>0.4</sub>NbS<sub>2-δ</sub>.

**Fig. S28** The density of states (DOS) of NbS<sub>2</sub>, Cu<sub>0.1</sub>NbS<sub>2</sub>, Cu<sub>0.4</sub>NbS<sub>2</sub> and Cu<sub>0.4</sub>NbS<sub>2-δ</sub>.

**Fig. S29** Schematic diagram of hydrogen spillover pathway 1 with different H adsorption sites in Cu<sub>0.4</sub>NbS<sub>2-δ</sub>.

**Fig. S30** Schematic diagram of hydrogen spillover pathway 2 with different H adsorption sites in Cu<sub>0.4</sub>NbS<sub>2-δ</sub>.

**Fig. S31** The calculated work functions ( $\Phi$ ) of (a) NbS<sub>2</sub>, (b) Cu<sub>0.1</sub>NbS<sub>2</sub>, (c) Cu<sub>0.4</sub>NbS<sub>2</sub> and (d) Cu<sub>0.4</sub>NbS<sub>2-δ</sub>.

**Fig. S32** The differences of work function ( $\Delta\Phi$ ) between the three intercalated phases (Cu<sub>0.1</sub>NbS<sub>2</sub>, Cu<sub>0.4</sub>NbS<sub>2</sub>, Cu<sub>0.4</sub>NbS<sub>2-δ</sub>) and NbS<sub>2</sub>. The calculated work functions are also shown inset.

**Fig. S33** The photographs of the catalyst and  $\text{WO}_3$  mixtures showing the change in color. The upper part is pristine  $\text{WO}_3$  coating before and after HER on indium tin oxide (ITO) electrode. The lower part is pristine mixture coating and mixture coating after HER on ITO electrode.

**Table S1** The lattice parameters of  $\text{Cu}_{0.1}\text{NbS}_2$  and  $\text{Cu}_{0.4}\text{NbS}_2$  from Rietveld refinements.

**Table S2** Normalized atomic ratios in  $\text{Cu}_{0.4}\text{NbS}_{2-\delta}$  as determined by XPS.

**Table S3** Comparison of HER activity for  $\text{Cu}_{0.4}\text{NbS}_{2-\delta}$  with other reported  $\text{NbS}_2$ -based electrocatalysts.

**Table S4** The  $\Delta G_{H^*}$  of different sites in  $\text{Cu}_{0.4}\text{NbS}_2$ .

## References

## Experimental details

### Characterization

Powder X-ray diffraction (PXRD) was performed at room temperature on a PANalytical Empyrean series 3 diffractometer equipped with Cu K $\alpha$  radiation ( $\lambda = 1.540598 \text{ \AA}$ ), operating at 45 kV and 40 mA and on a diffracted-beam graphite monochromator in scanning mode (step =  $0.01313^\circ 2\theta$ ). The electron paramagnetic resonance spectrometry (EPR) was carried using a Bruker EMX plus-6/1 spectrometer at room temperature. The Raman spectra was collected on a micro-Raman spectrometer (HORIBA HR Evolution) using a 532 nm laser as the excitation source. The morphology of sample was imaged by scanning electron microscopy (SEM, Hitachi S-4800) and high-resolution transmission electron microscopy (HRTEM, JEM-2200FS, JEOL). The selected area electron diffraction (SAED) and the component analysis were performed by field-emission transmission electron microscope equipped with an energy-dispersive X-ray spectroscopy (EDS) analyzer. The X-ray photoelectron spectroscopy (XPS) spectra were acquired from an X-ray photoelectron spectrophotometer (Thermo Scientific K-Alpha) using Al K $\alpha$  radiation source ( $h\nu = 1486.6 \text{ eV}$ ). The hydrogen temperature-programmed desorption (H<sub>2</sub>-TPD) measurement was carried out by using Micromeritics AutoChem II 2920, USA. Typically, 50 mg sample was treated at 50 °C in 10 % H<sub>2</sub>/Ar mixed gas for 1 h to reach the H<sub>2</sub> saturation. Then the sample was cleaned by Ar gas at 50 °C for 30 min to remove weakly adsorbed H<sub>2</sub> on the sample surface, and finally heated from 50 to 800 °C (10 °C/min of heating rate) in Ar atmosphere for desorption.

### Electrochemical measurements

All the electrochemical measurements were performed on a CHI 660E electro-chemistry workstation (CH, Shanghai, China) with a standard three-electrode setup using Ag/AgCl as the reference electrode, a graphite rod as the counter electrode, and a clean glassy carbon electrode (GCE) coated with drop-cast catalysts as the working electrode. To prepare working electrode, 5 mg of the as-prepared catalysts and 5  $\mu\text{L}$  5 wt % Nafion solutions were ultrasonically dispersed in DI water-ethanol solution (450  $\mu\text{L}$ +545  $\mu\text{L}$ ) to form a homogeneous catalyst ink. Then 10  $\mu\text{L}$  catalyst ink was drop-casted onto GCE with a geometric area of 0.1256 cm<sup>2</sup>. The loading amount of catalyst was calculated to

be 398  $\mu\text{g}/\text{cm}^2$ . All the measurements were performed in a  $\text{N}_2$ -saturated 0.5 M  $\text{H}_2\text{SO}_4$  aqueous solution. HER polarization curves were obtained by the linear sweep voltammetry (LSV) with a scan rate of 5 mV/s, which were recorded on a rotating disk electrode (RDE) with constant rotation speeds of 1600 rpm to eliminate the bubbles. The Tafel plots were derived from the corresponding LSV curves based on the Tafel equation. The electrochemical impedance spectra (EIS) were obtained over a frequency range from  $10^6$  to 0.1 Hz. The electrochemical double-layer capacitance ( $C_{\text{dl}}$ ) was performed from the cyclic voltammetry curves (CV) within non-Faradaic region, with the scan rate from 20 to 200 mV/s. The electrochemical stability of the catalyst was evaluated by cycling the electrodes for 3000th times. All the potentials reported in this work were calibrated against and converted to the reversible hydrogen electrode (RHE) after iR-corrected:  $E(\text{RHE}) = E(\text{Ag}/\text{AgCl}) + 0.0591 \times \text{pH} + 0.197$ .

### Theoretical calculations

The first-principle calculations were carried out using ab initio density functional theory (DFT) as implemented in the VASP codes,<sup>1</sup> where Perdew–Burke–Ernzerhof (PBE) exchange and correlation functional form of the generalized gradient approximation (GGA) were utilized.<sup>2</sup> The plane-wave cutoff energy was fixed at 450 eV. The energy convergence between two consecutive self-consistent steps was set to  $10^{-6}$  eV. The atomic positions and lattice parameters were optimized, until the total force acting on each atom (Hellman-Feynman forces) was lower than 0.01 eV/Å. The crystal structure of 3R-NbS<sub>2</sub> was taken from the ICSD database. The crystal structure of  $\text{Cu}_{0.4}\text{NbS}_2$  from Rietveld refinement result was modified according to the experimental results to obtain the calculation model of  $\text{Cu}_{0.4}\text{NbS}_{2-\delta}$ . The optimized lattice parameters of all materials were taken from the experimental results. Monkhorst-Pack k-points of  $6 \times 6 \times 1$  was applied for all the surface calculations. A thickness of vacuum was adopted as 15 Å along z-axis. The Gibbs free energy change ( $\Delta G_{\text{H}^*}$ ) for HER was calculated according to this formula:  $\Delta G_{\text{H}^*} = \Delta E_{\text{H}^*} + \Delta E_{\text{ZPE}} - T\Delta S$ , where  $\Delta E_{\text{H}^*}$  is the hydrogen adsorption energy,  $\Delta E_{\text{H}^*} = E_{(\text{surface}+\text{H}^*)} - E_{\text{surface}} - 1/2 E_{\text{H}_2}$ ,  $E_{(\text{surface}+\text{H}^*)}$  and  $E_{\text{surface}}$  are overall energy of the surface model with and without  $\text{H}^*$  adsorption, respectively;  $\Delta E_{\text{ZPE}}$  is the zero-point energy difference that obtained by

vibrational frequency calculation;  $\Delta S$  is the entropy difference between the adsorbed state and the gas phase, and  $T$  is the system temperature (298.15 K in this work).

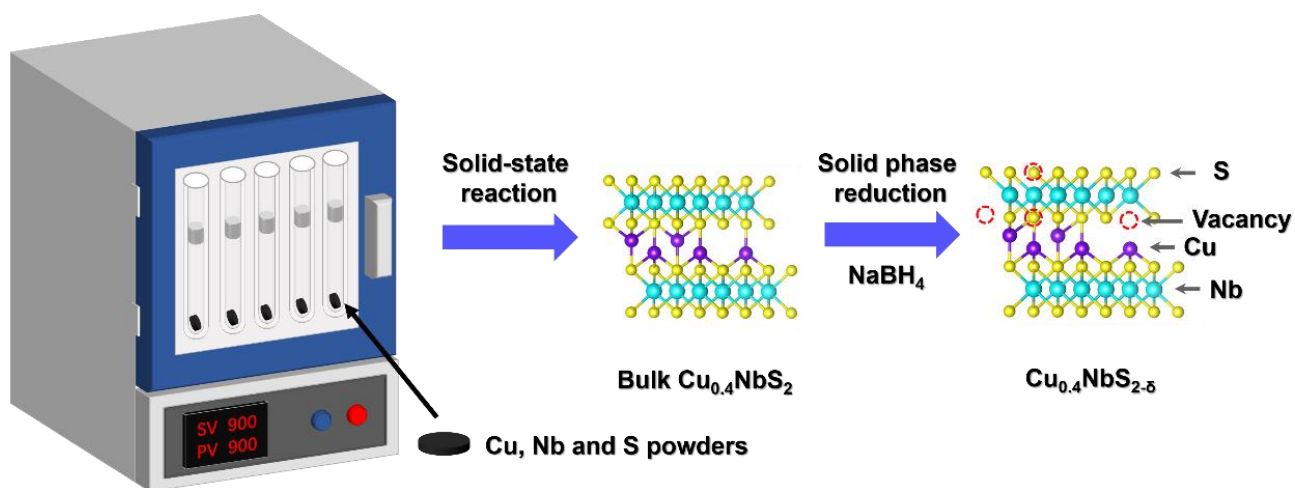


**Fig. S1** Schematic diagram of the synthesis process of  $\text{Cu}_{0.4}\text{NbS}_2$  and  $\text{Cu}_{0.4}\text{NbS}_{2-\delta}$  polycrystalline samples.

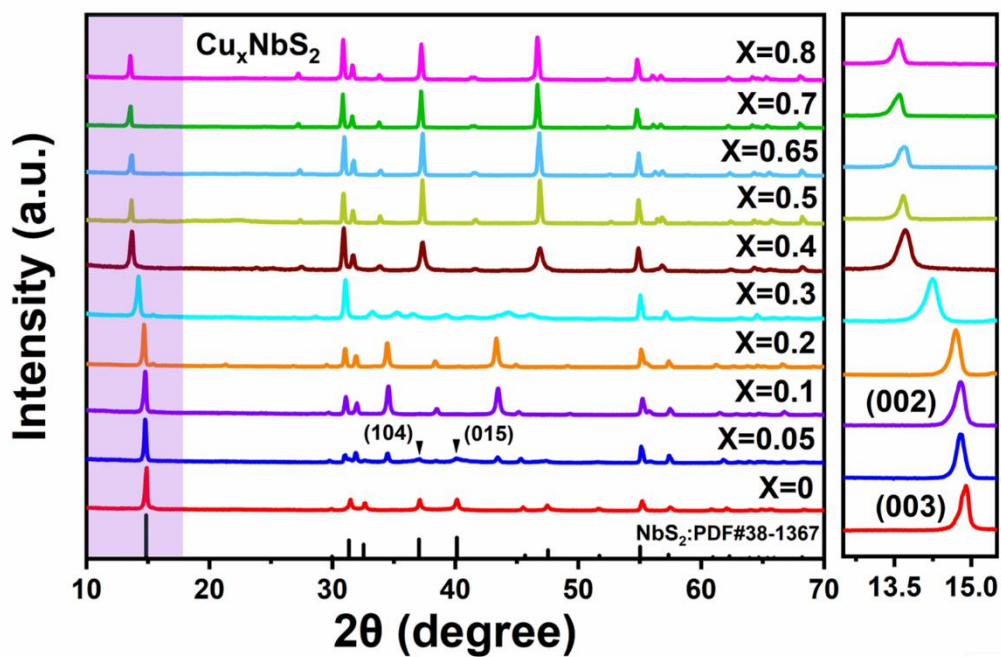


**Fig. S2** The XRD patterns of  $\text{Cu}_x\text{NbS}_2$  ( $x = 0, 0.05, 0.1, 0.2, 0.3, 0.4, 0.5, 0.65, 0.7$  and  $0.8$ ). The right part shows the enlarged (002)/(003) diffraction peaks of the samples.

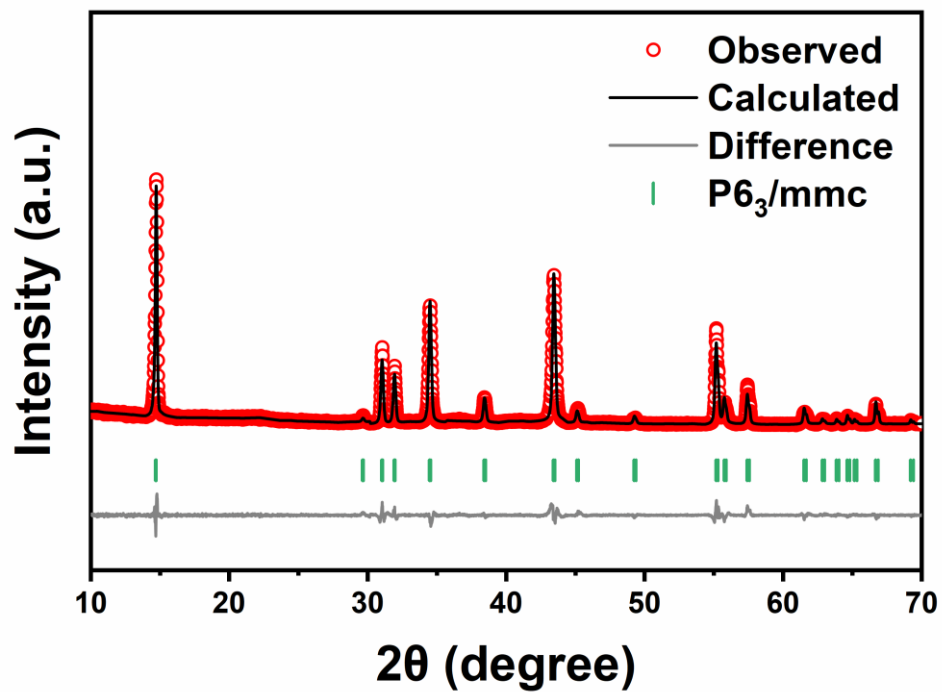


**Fig. S3** Rietveld refinement of the PXRD pattern of  $\text{Cu}_{0.1}\text{NbS}_2$ .

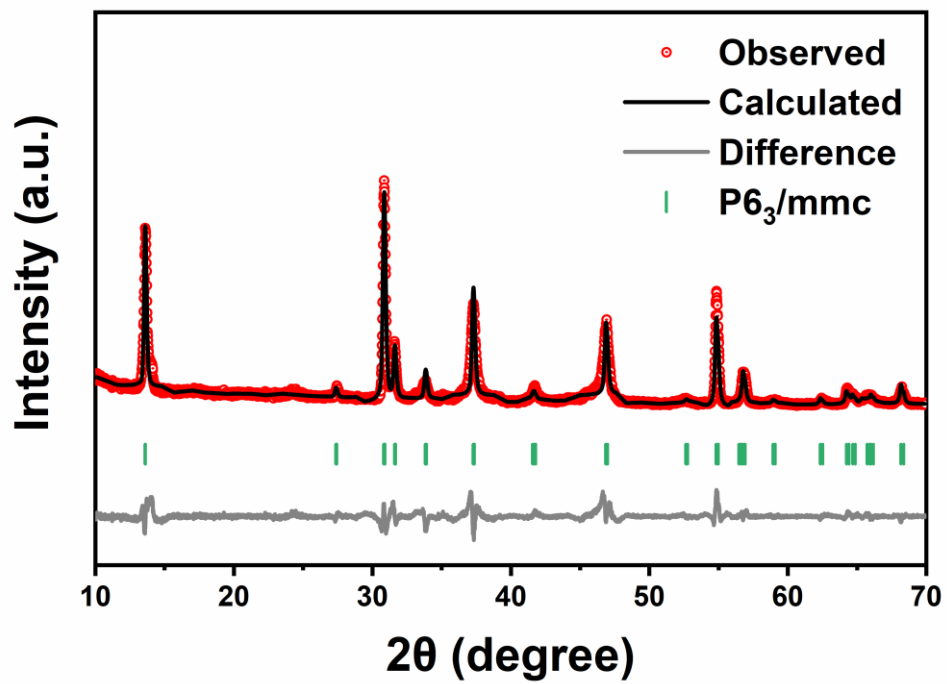


**Fig. S4** Rietveld refinement of the PXRD pattern of  $\text{Cu}_{0.4}\text{NbS}_2$ .

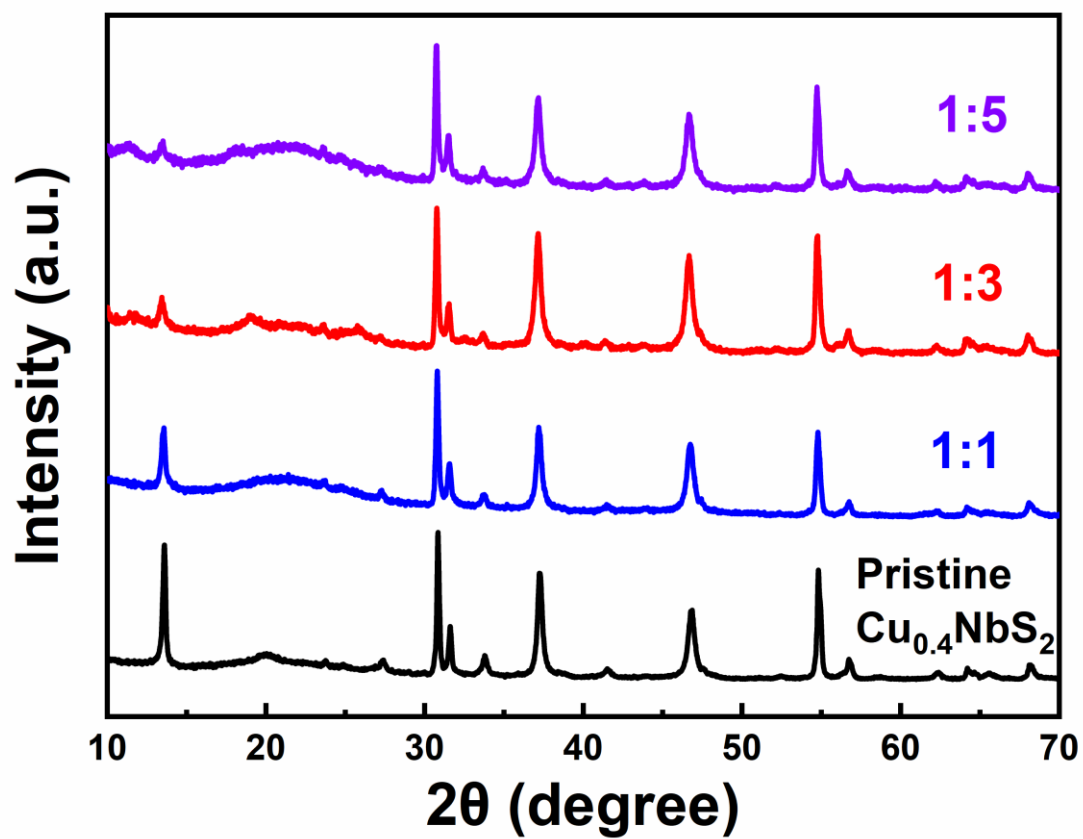


**Fig. S5** The XRD patterns of  $\text{Cu}_{0.4}\text{NbS}_{2-\delta}$  with different mass ratios of  $\text{Cu}_{0.4}\text{NbS}_2 : \text{NaBH}_4 = 1:1, 1:3$  and  $1:5$ .

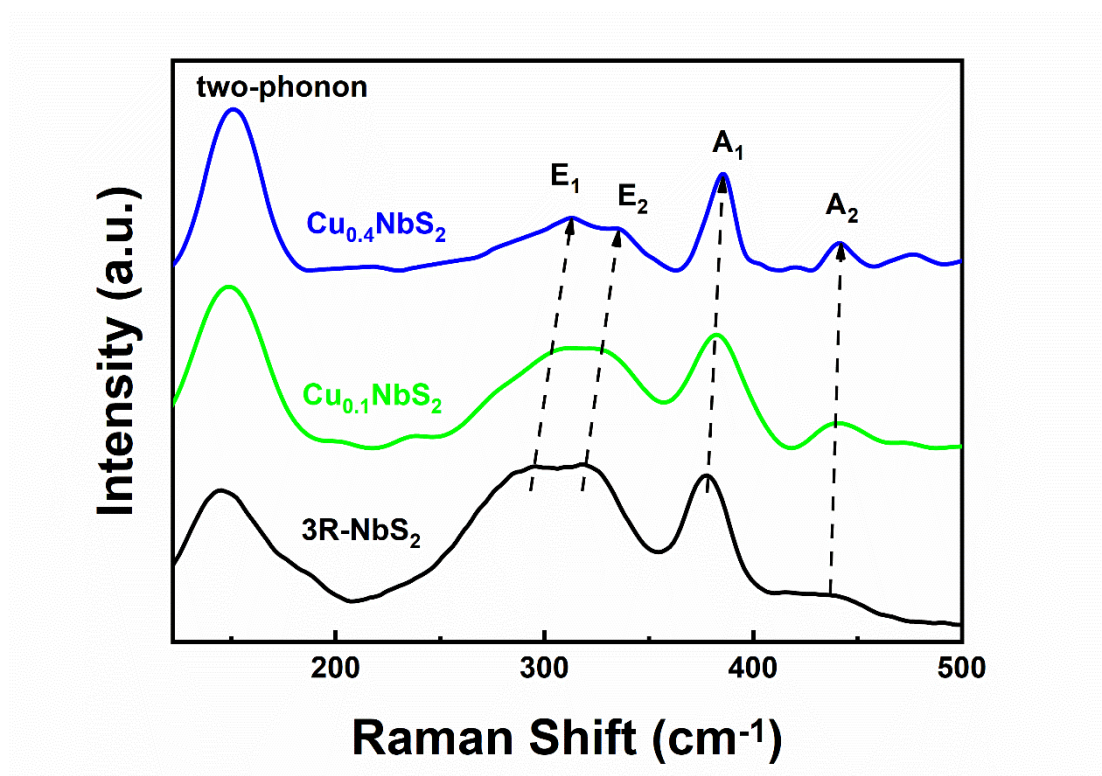


**Fig. S6** Raman spectra of 3R-NbS<sub>2</sub>, Cu<sub>0.1</sub>NbS<sub>2</sub> and Cu<sub>0.4</sub>NbS<sub>2</sub>. The spectra of 3R-NbS<sub>2</sub> and Cu<sub>0.4</sub>NbS<sub>2</sub> were also used in the main text in Fig. 1d.

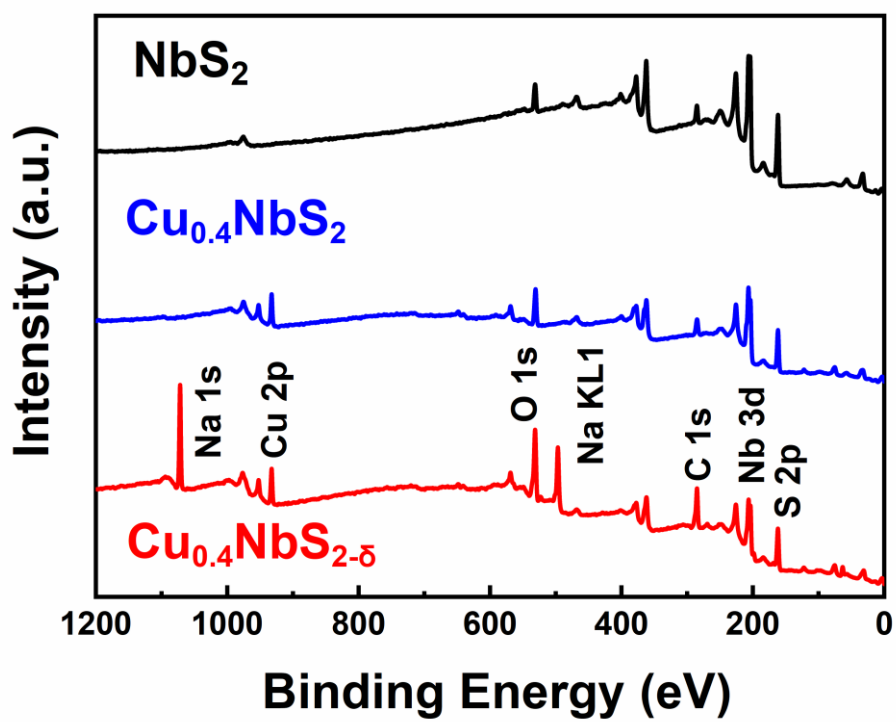


**Fig. S7** Full XPS spectra of 3R-NbS<sub>2</sub>, Cu<sub>0.4</sub>NbS<sub>2</sub> and Cu<sub>0.4</sub>NbS<sub>2-δ</sub>.

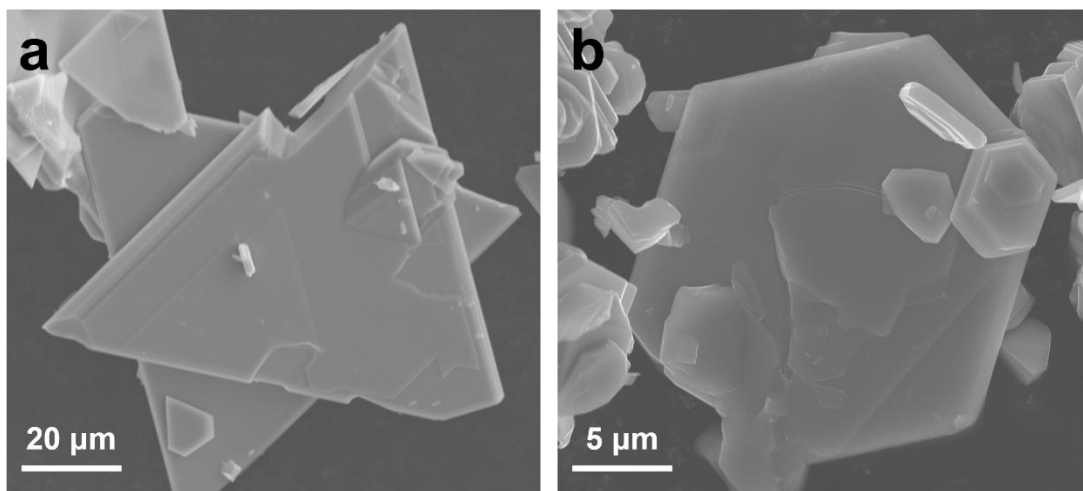


**Fig. S8** The SEM images of (a) NbS<sub>2</sub> and (b) Cu<sub>0.4</sub>NbS<sub>2</sub>.

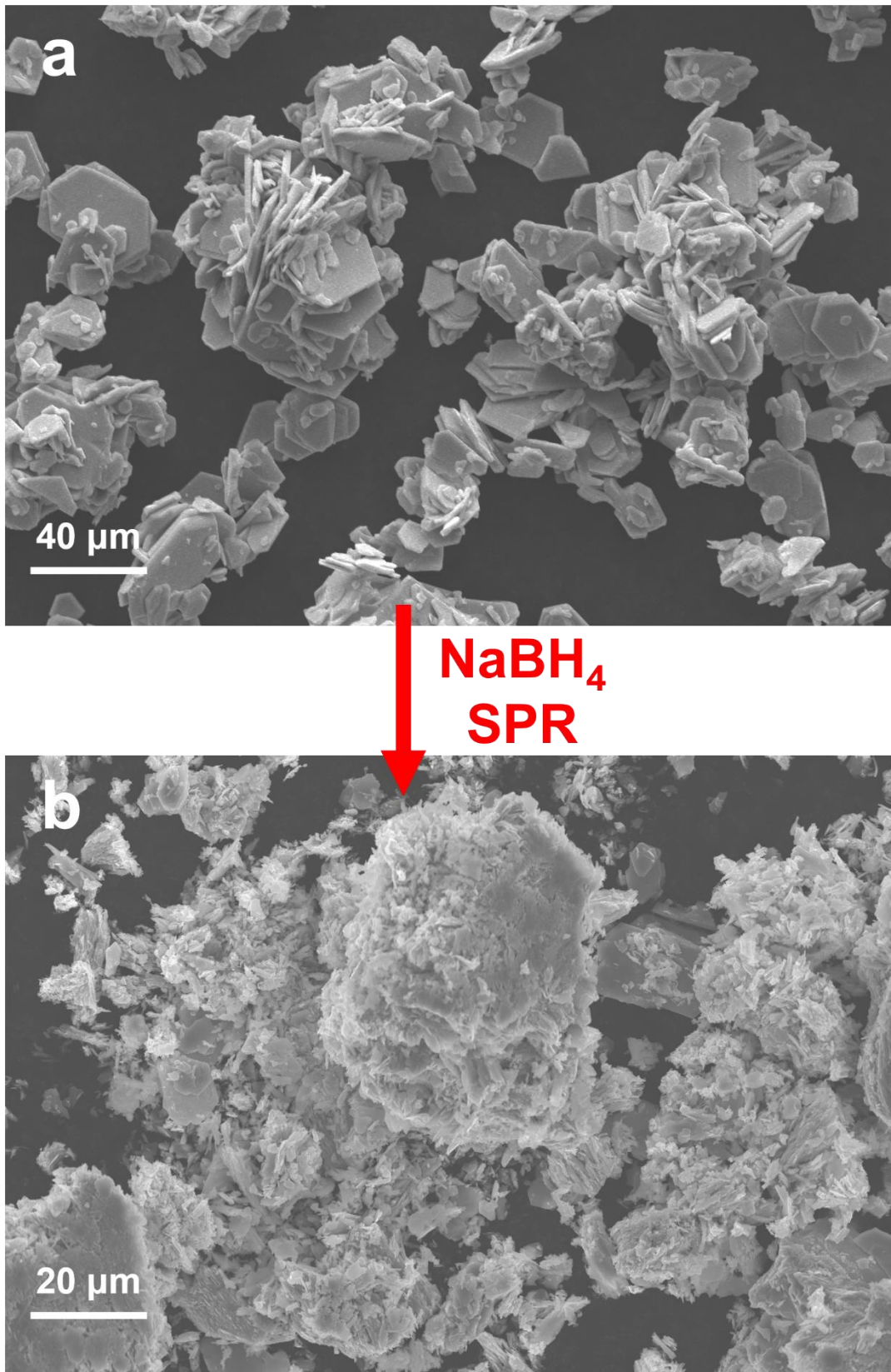


**Fig. S9** The SEM images of  $\text{Cu}_{0.4}\text{NbS}_2$  (a) before and (b) after SPR.

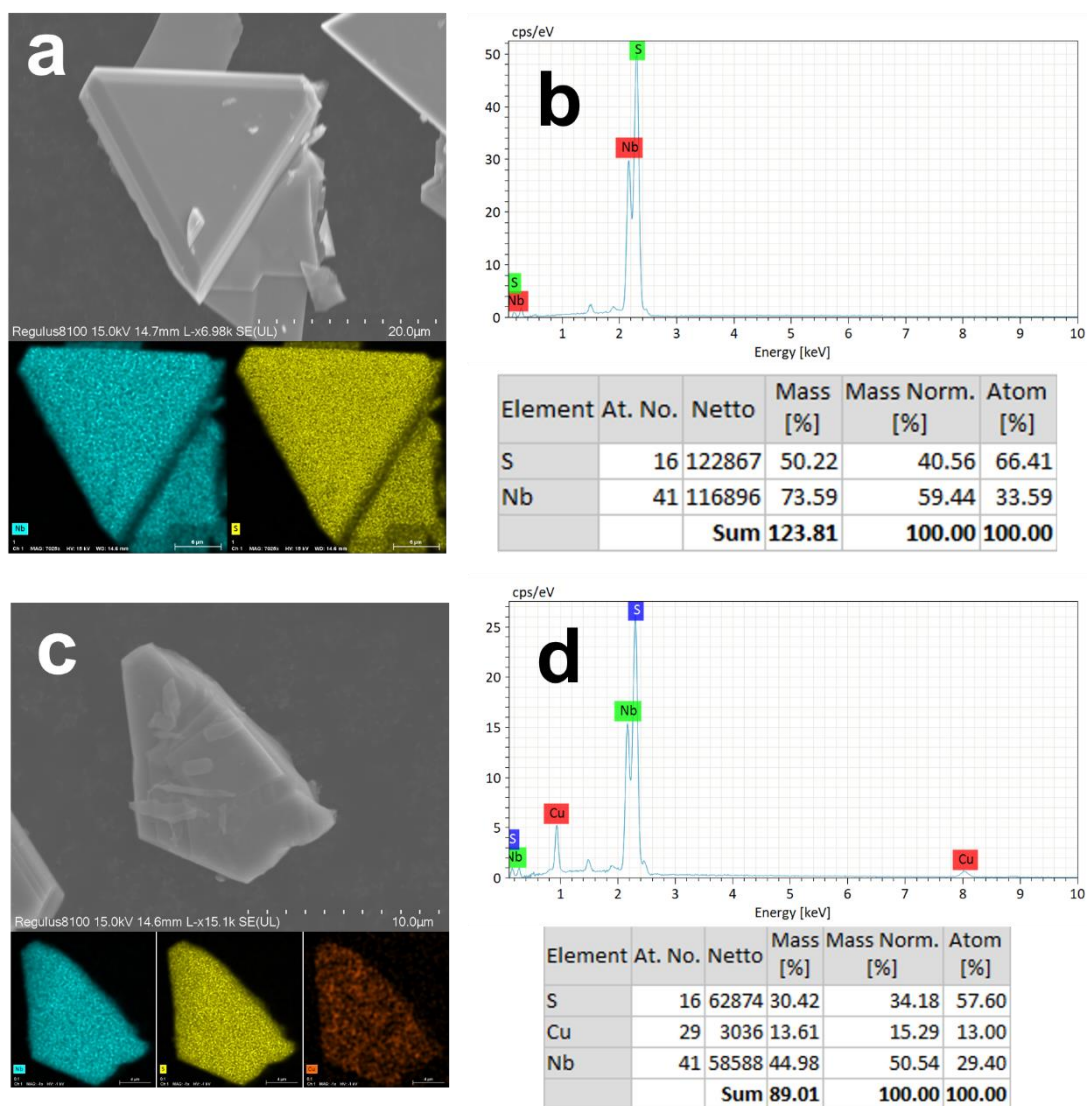


**Fig. S10** (a) The SEM image and the elemental mapping of NbS<sub>2</sub>; (b) The EDS results of NbS<sub>2</sub>; (c) the SEM image and the elemental mapping of Cu<sub>0.4</sub>NbS<sub>2</sub>; (d) The EDS results of Cu<sub>0.4</sub>NbS<sub>2</sub>.

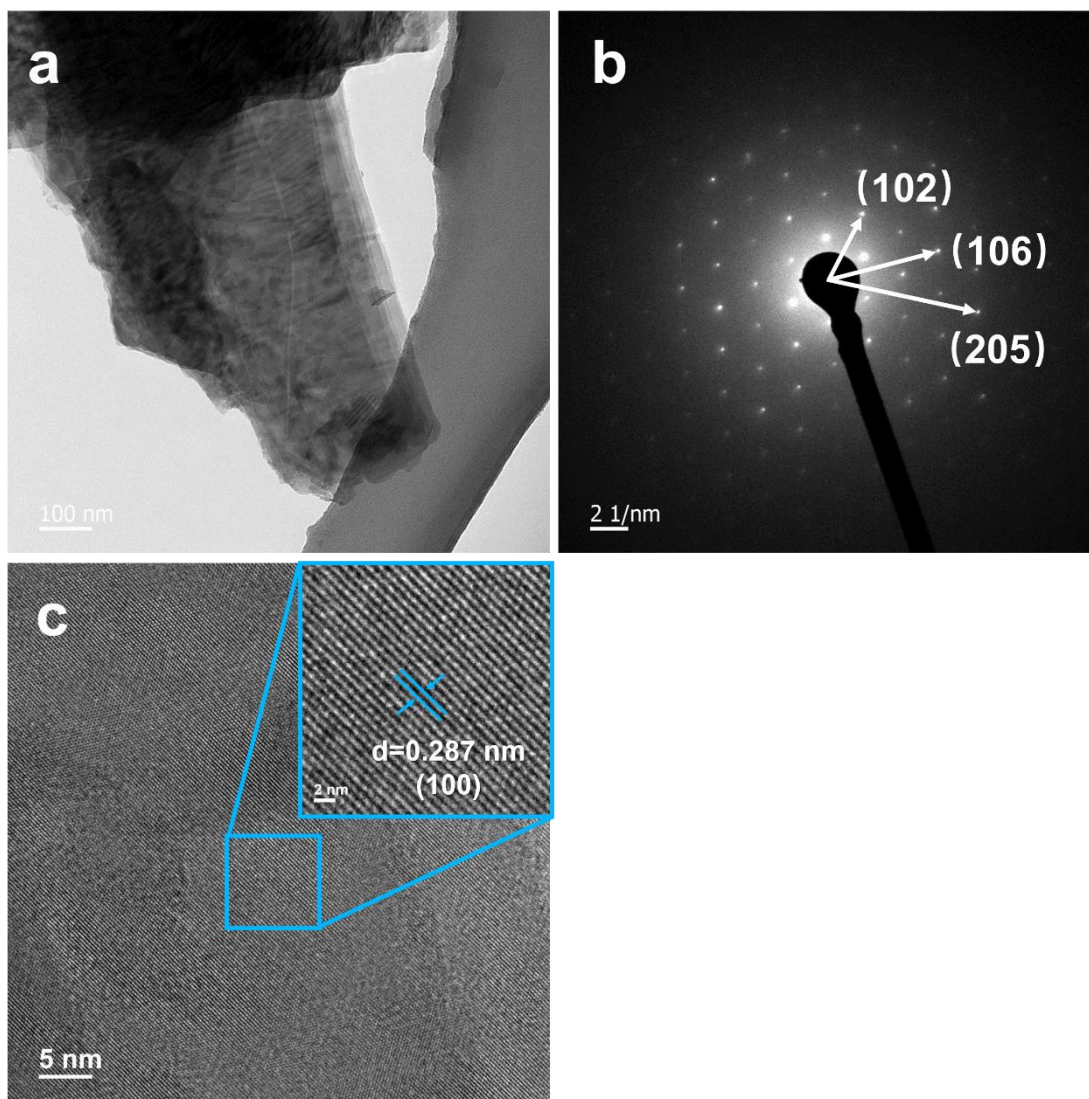


**Fig. S11** (a) The TEM image of  $\text{Cu}_{0.4}\text{NbS}_2$ ; (b) The corresponding SAED pattern; (c) The HRTEM images of  $\text{Cu}_{0.4}\text{NbS}_2$ .

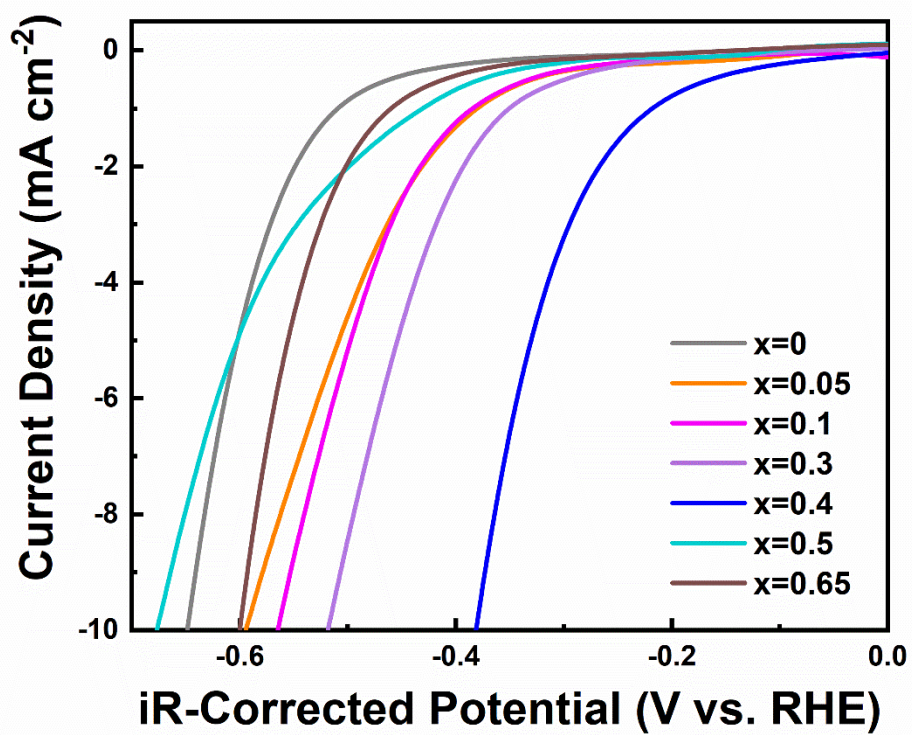


**Fig. S12** HER polarization curves of the  $\text{Cu}_x\text{NbS}_2$  ( $x = 0, 0.05, 0.1, 0.2, 0.3, 0.4, 0.5$  and  $0.65$ ).

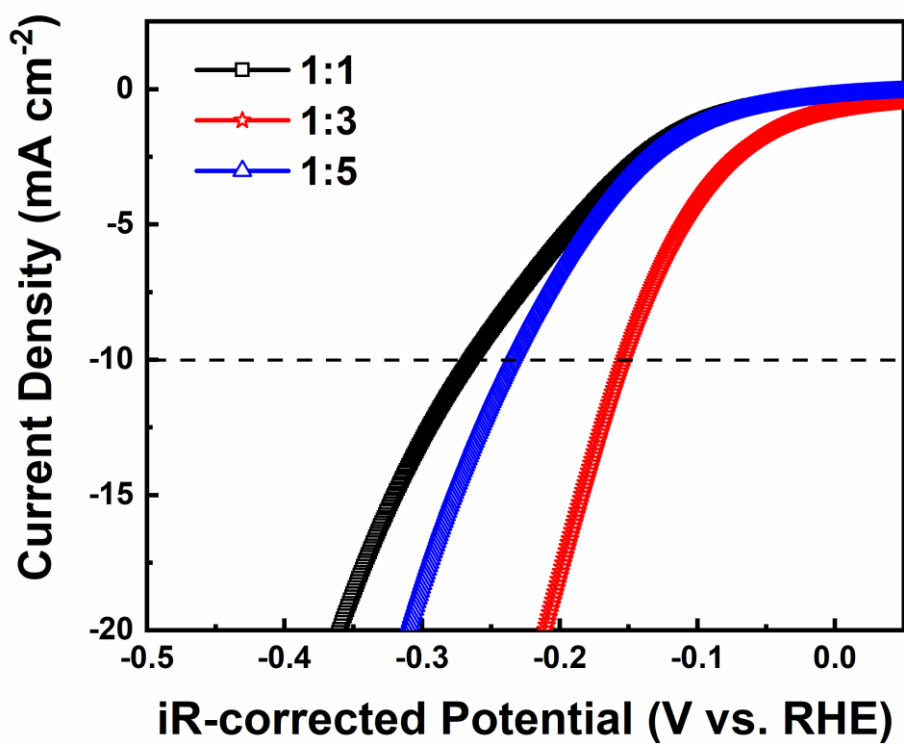


**Fig. S13** HER polarization curves of  $\text{Cu}_{0.4}\text{NbS}_{2-\delta}$  with different mass ratios of  $\text{Cu}_{0.4}\text{NbS}_2$  :  $\text{NaBH}_4 = 1:1$ , 1:3 and 1:5.

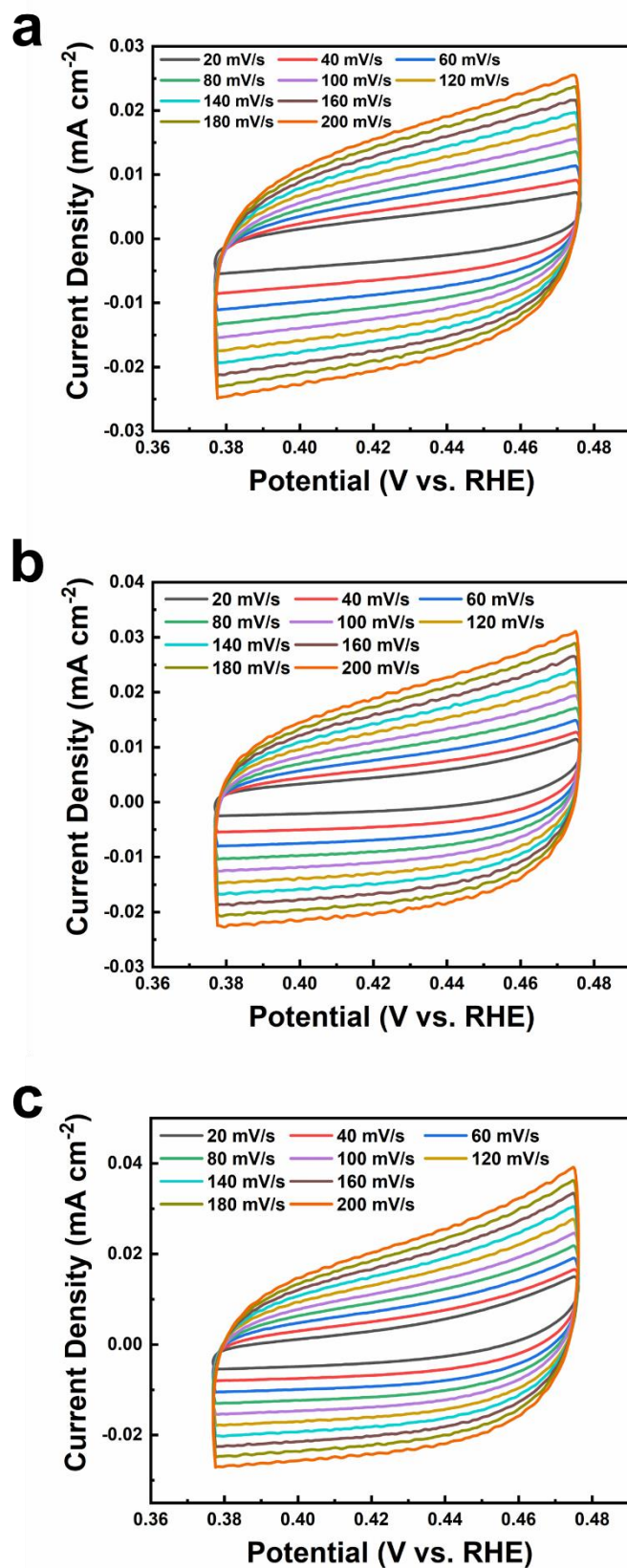


**Fig. S14** CV curves measured at different scan rates of (a)  $\text{NbS}_2$ , (b)  $\text{Cu}_{0.4}\text{NbS}_2$ , and (c)  $\text{Cu}_{0.4}\text{NbS}_{2-\delta}$ .

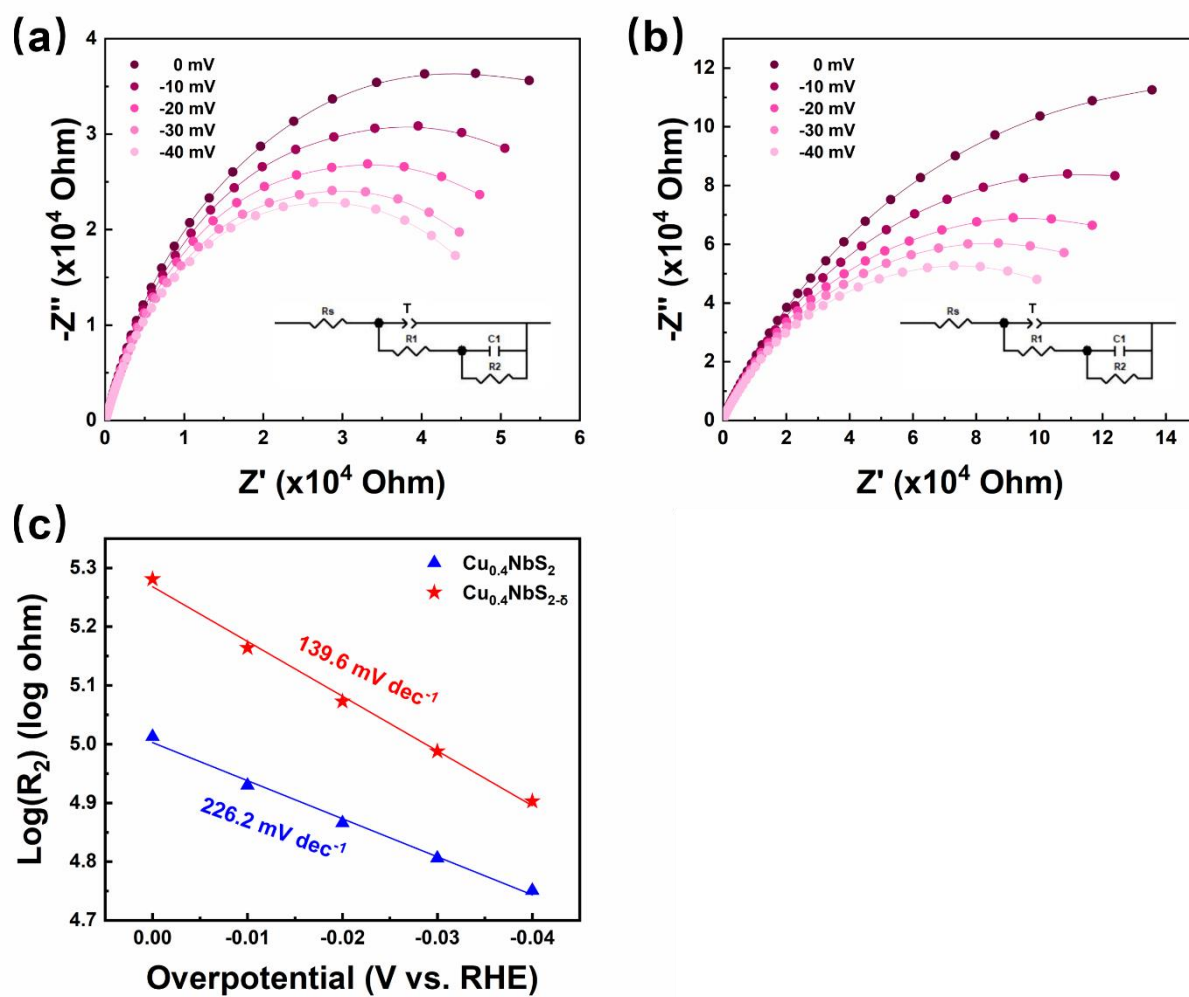


**Fig. S15** Nyquist plot for (a)  $\text{Cu}_{0.4}\text{NbS}_2$  and (b)  $\text{Cu}_{0.4}\text{NbS}_{2-\delta}$  catalyst at various HER overpotentials (Inset shows the equivalent circuit for the simulation); (c) EIS-derived Tafel plots of the  $\text{Cu}_{0.4}\text{NbS}_2$  and  $\text{Cu}_{0.4}\text{NbS}_{2-\delta}$  catalysts obtained from the hydrogen adsorption resistance  $R_2$ .

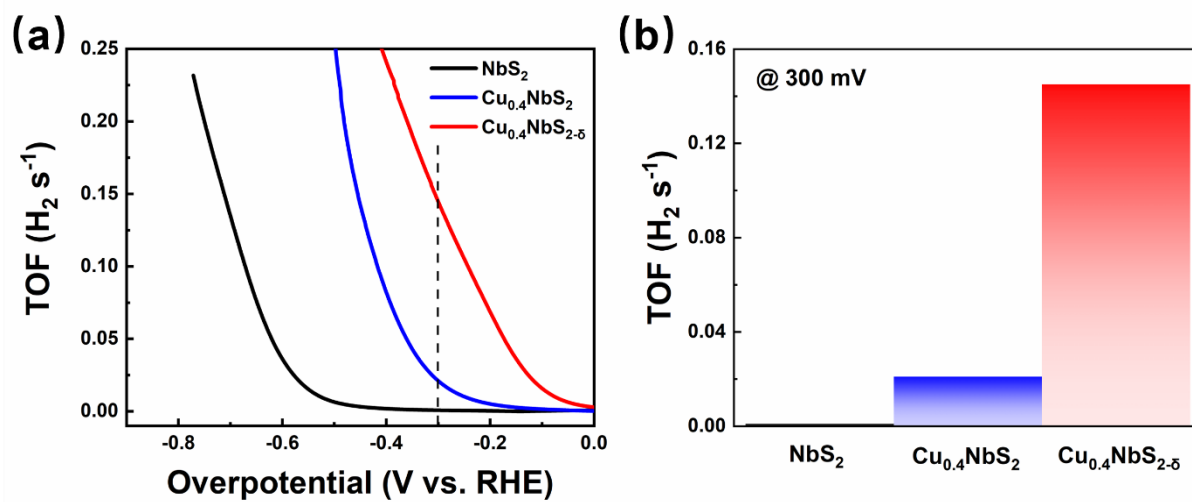


**Fig. S16** (a) Turnover frequency (TOF) of  $\text{NbS}_2$ ,  $\text{Cu}_{0.4}\text{NbS}_2$  and  $\text{Cu}_{0.4}\text{NbS}_{2-\delta}$ ; (b) TOF of  $\text{NbS}_2$ ,  $\text{Cu}_{0.4}\text{NbS}_2$  and  $\text{Cu}_{0.4}\text{NbS}_{2-\delta}$  at an overpotential of 300 mV for the HER.

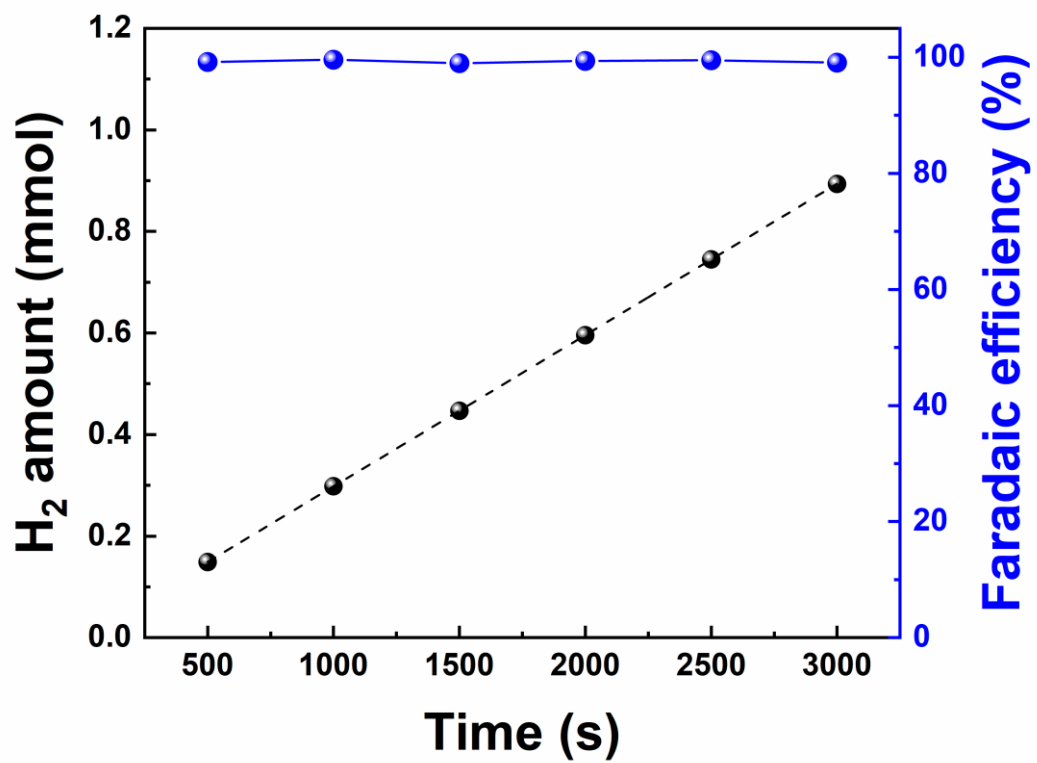


**Fig. S17** Faradaic efficiency of H<sub>2</sub> production upon operation time.

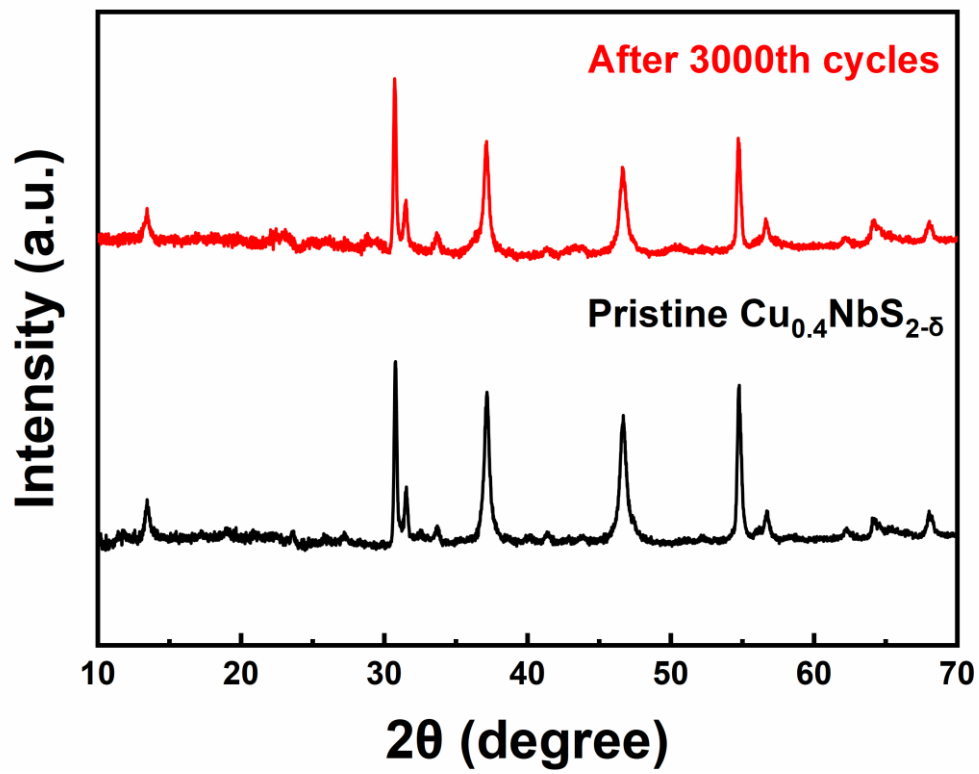


**Fig. S18** The XRD patterns of  $\text{Cu}_{0.4}\text{NbS}_{2-\delta}$  before and after 3000th cycles.

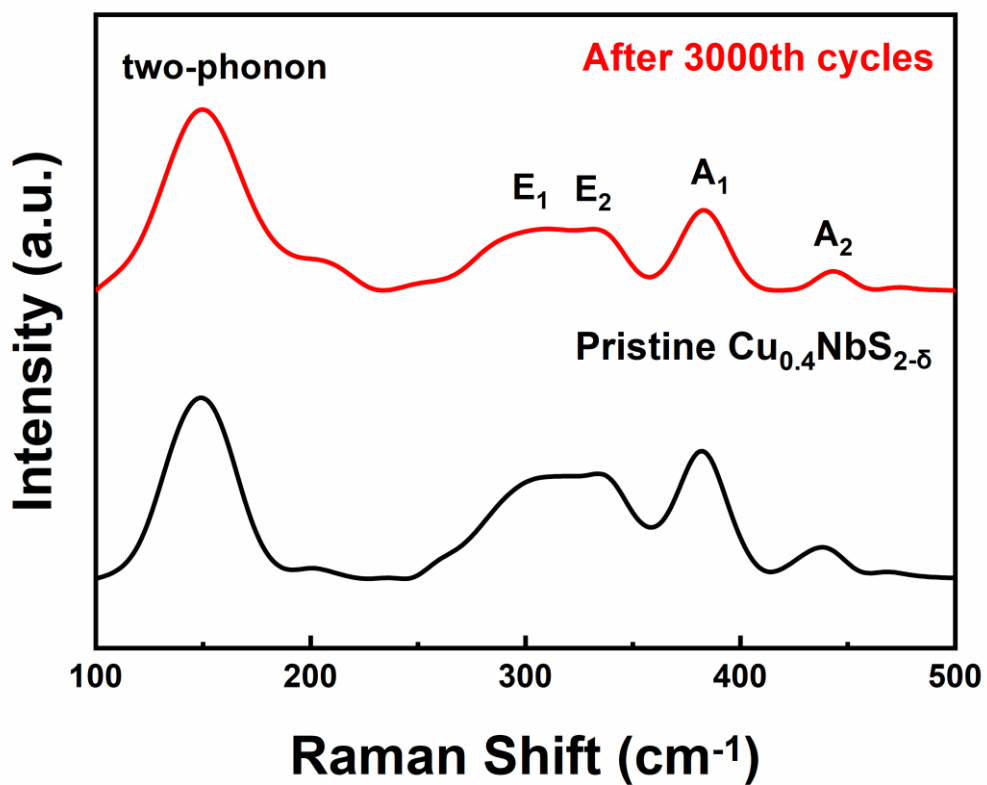


**Fig. S19** Raman spectra of Cu<sub>0.4</sub>NbS<sub>2-δ</sub> before and after 3000th cycles.

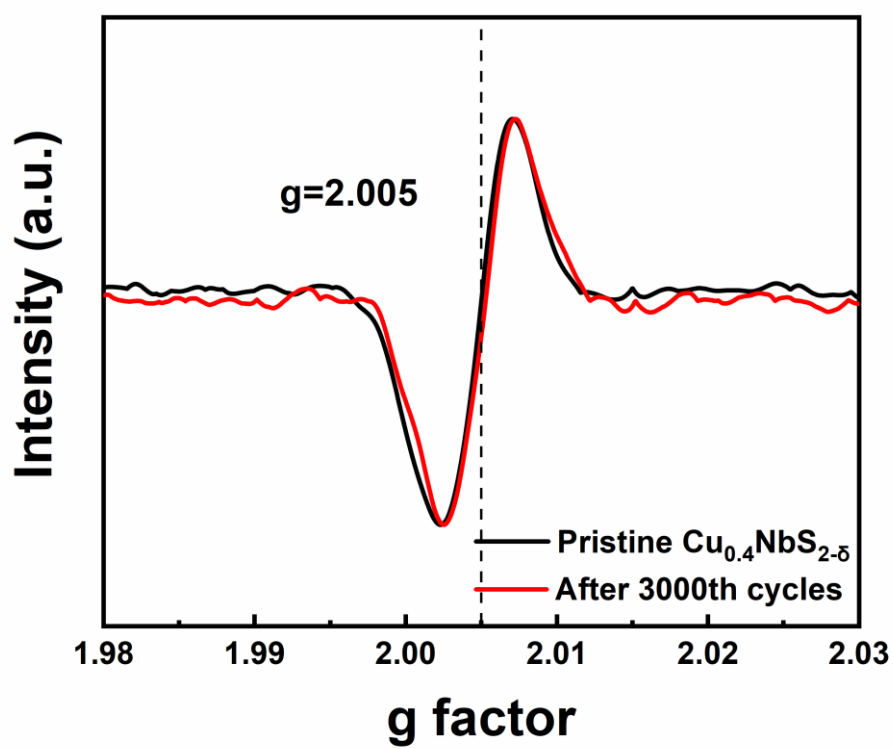


**Fig. S20** EPR spectra of  $\text{Cu}_{0.4}\text{NbS}_{2.8}$  before and after 3000th cycles.

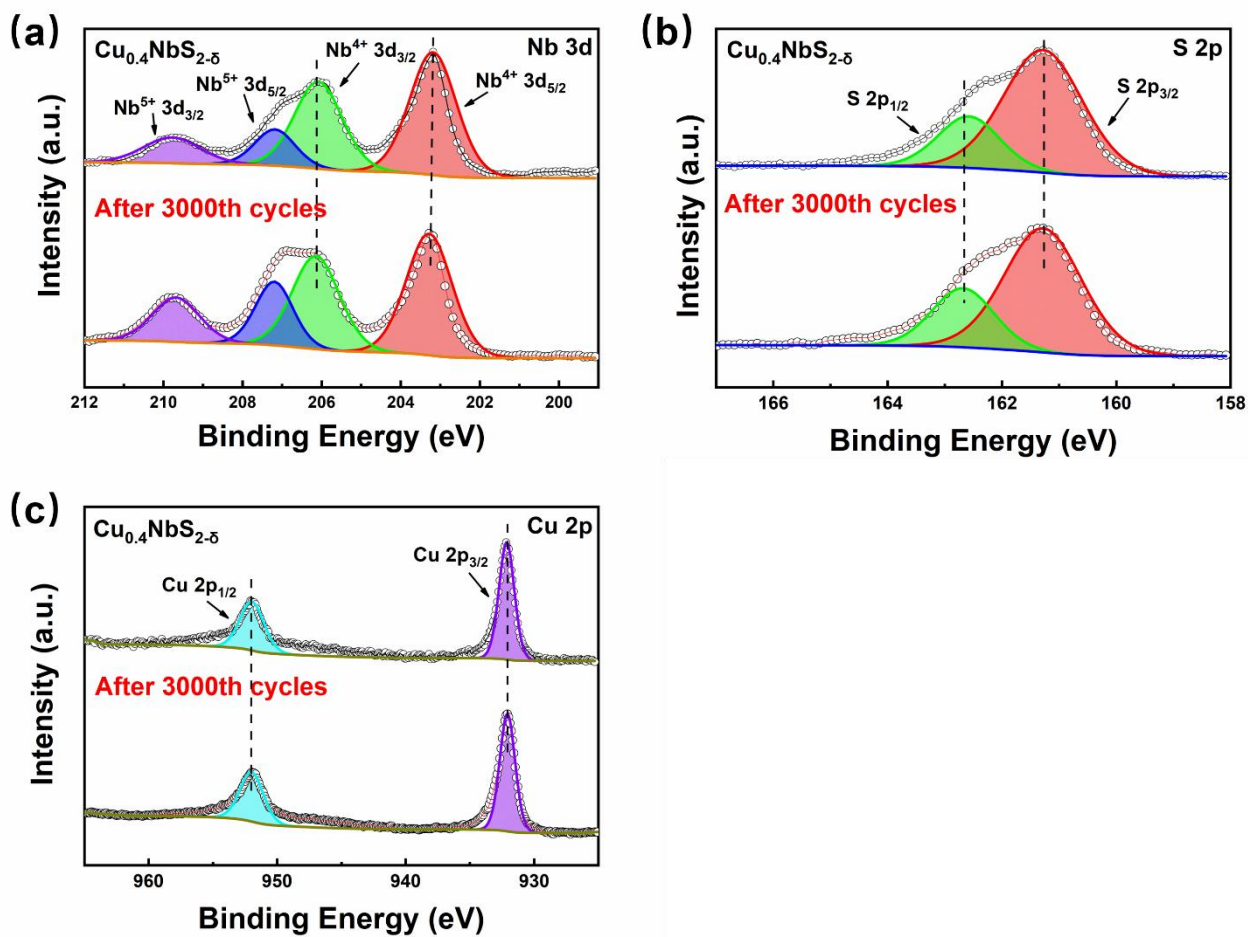


**Fig. S21** High resolution XPS spectra of (a) Nb 3d, (b) S 2p and (c) Cu 2p in  $\text{Cu}_{0.4}\text{NbS}_{2-\delta}$  before and after 3000th cycles.

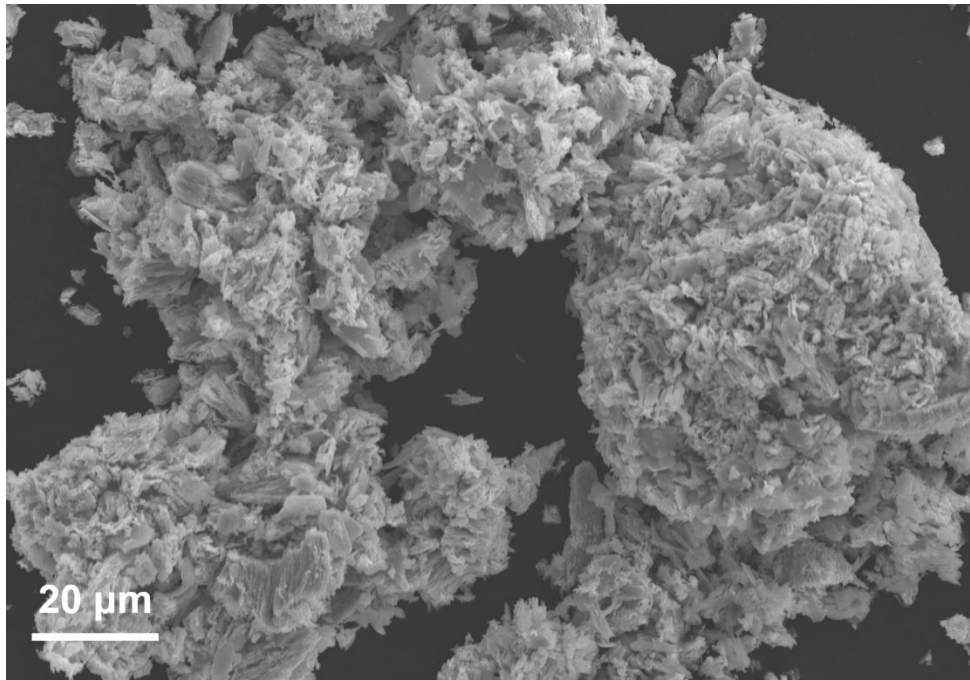


**Fig. S22** The SEM image of Cu<sub>0.4</sub>NbS<sub>2-δ</sub> after 3000th cycles.

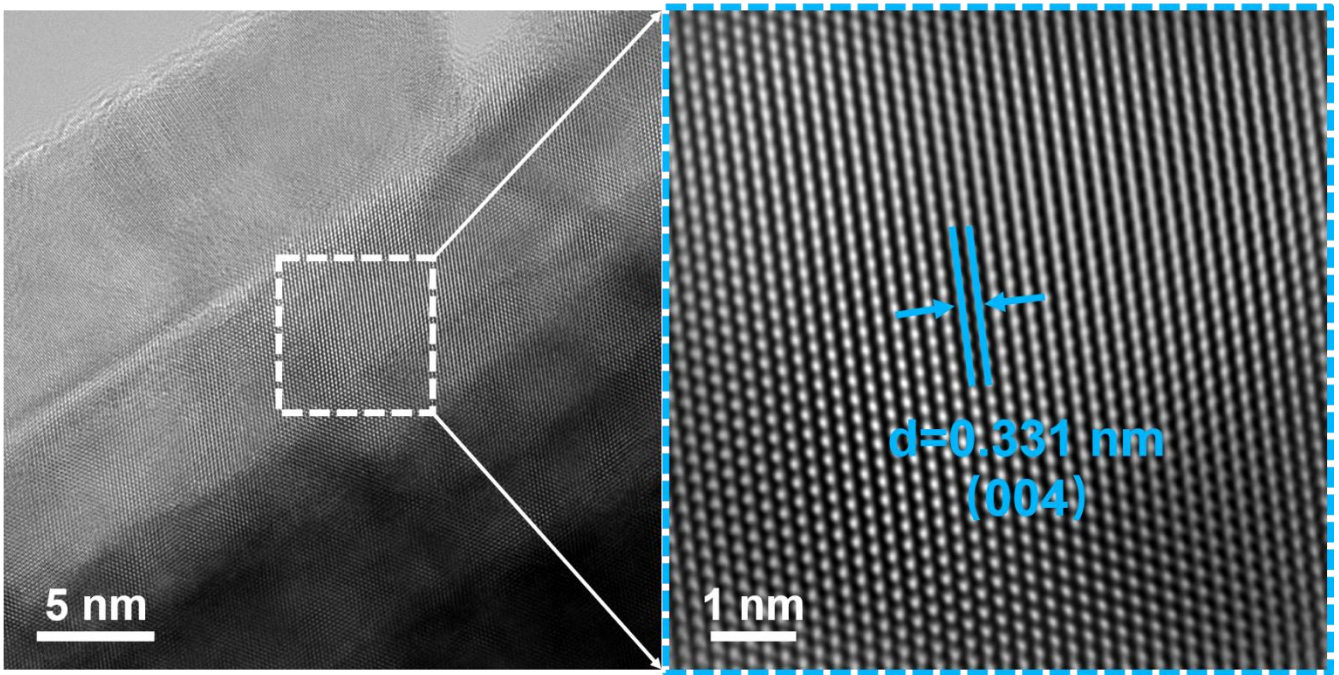


**Fig. S23** The TEM images of  $\text{Cu}_{0.4}\text{NbS}_{2-\delta}$  after 3000th cycles.

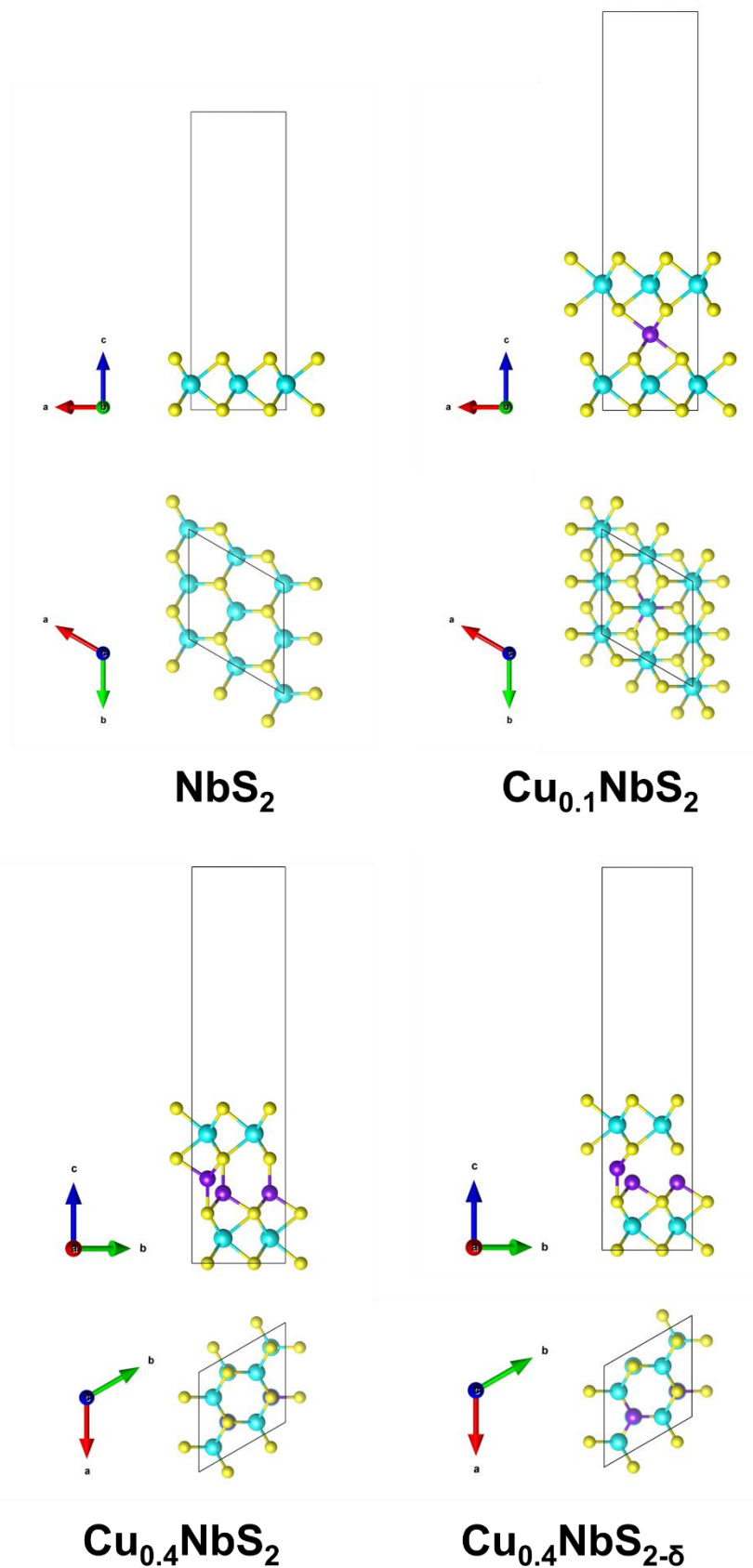


**Fig. S24** The single layer models of NbS<sub>2</sub>, Cu<sub>0.1</sub>NbS<sub>2</sub>, Cu<sub>0.4</sub>NbS<sub>2</sub> and Cu<sub>0.4</sub>NbS<sub>2-δ</sub> for calculation.

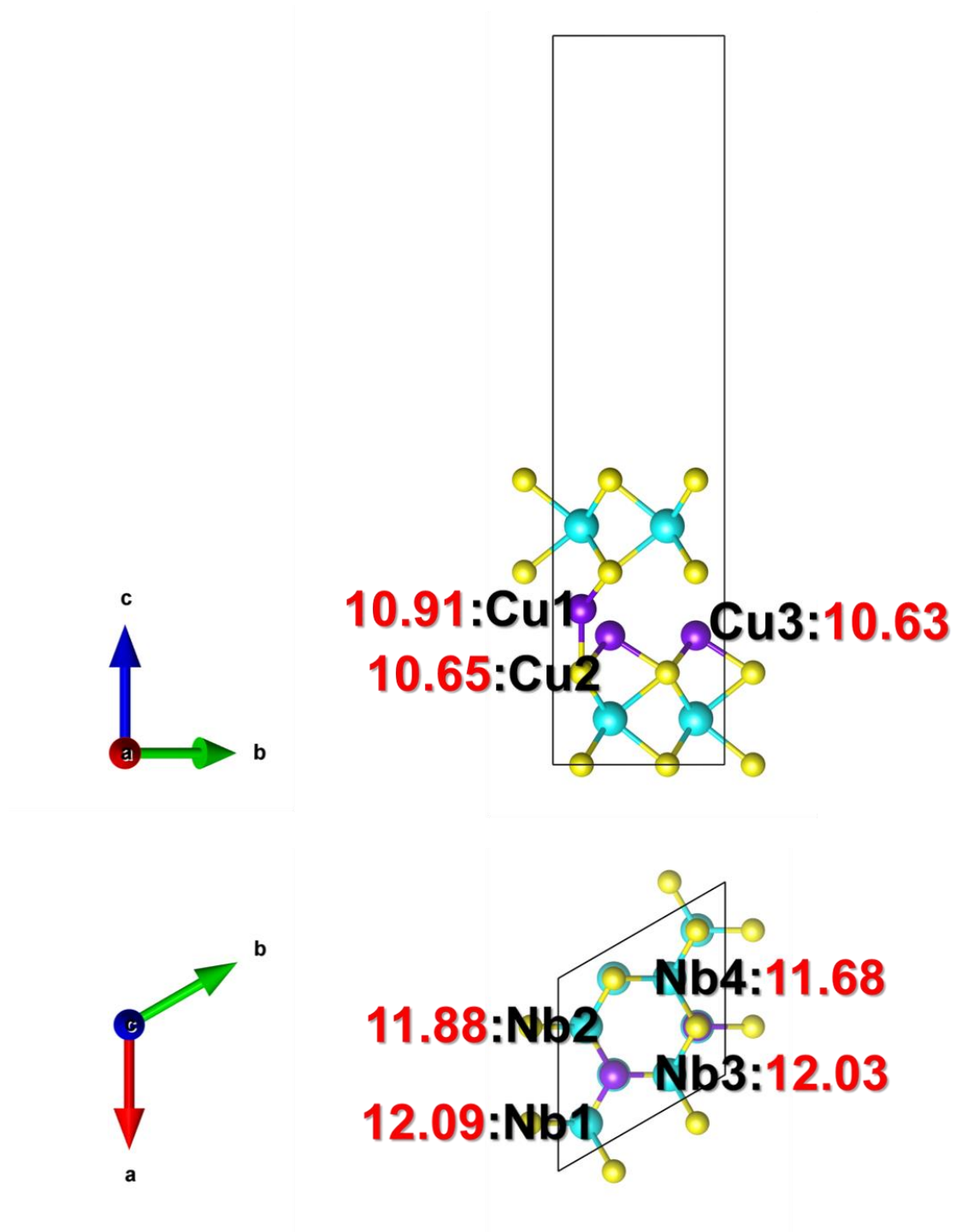


**Fig. S25** The Bader charge of different Nb and Cu sites in  $\text{Cu}_{0.4}\text{NbS}_{2-\delta}$  after the S vacancy induced.

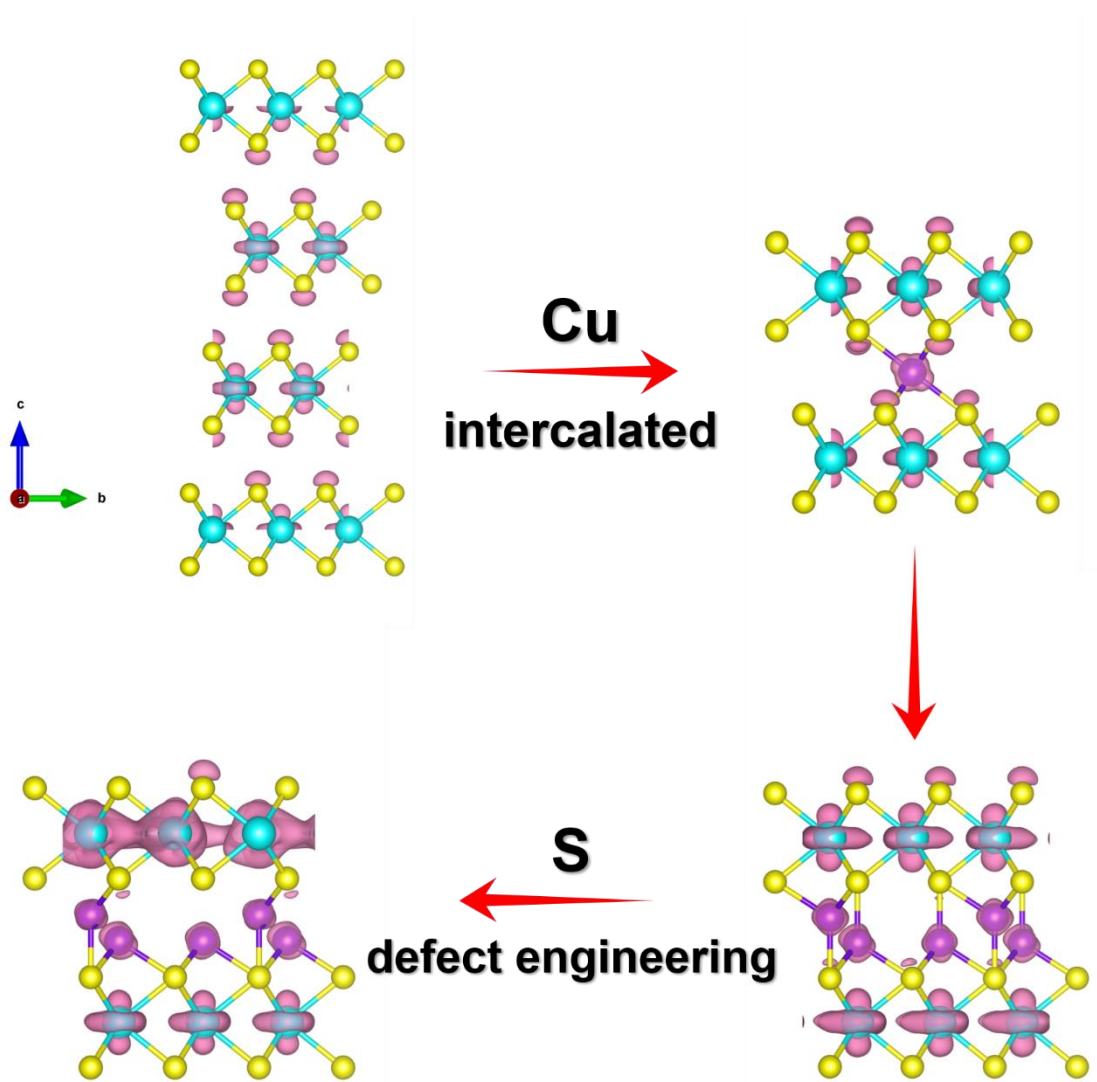


**Fig. S26** Partial charge density of NbS<sub>2</sub>, Cu<sub>0.1</sub>NbS<sub>2</sub>, Cu<sub>0.4</sub>NbS<sub>2</sub> and Cu<sub>0.4</sub>NbS<sub>2-δ</sub> within 1.0 eV below Fermi level.

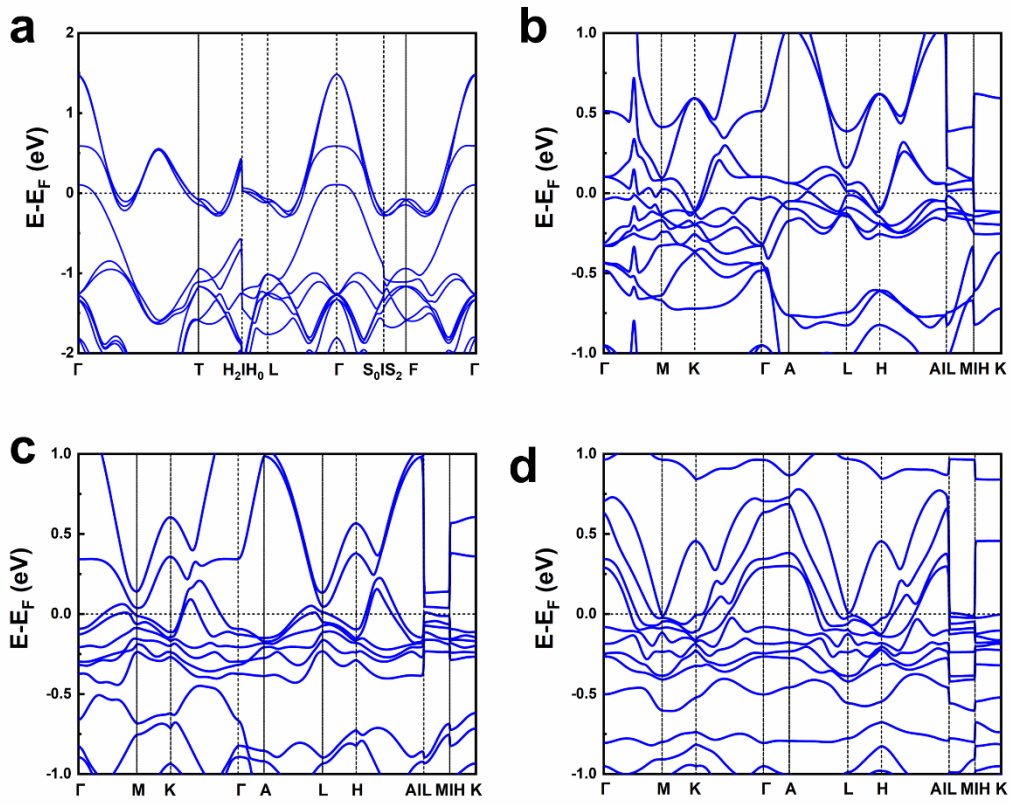


**Fig. S27** The band structures of (a)  $\text{NbS}_2$ , (b)  $\text{Cu}_{0.1}\text{NbS}_2$ , (c)  $\text{Cu}_{0.4}\text{NbS}_2$  and (d)  $\text{Cu}_{0.4}\text{NbS}_{2-\delta}$ .

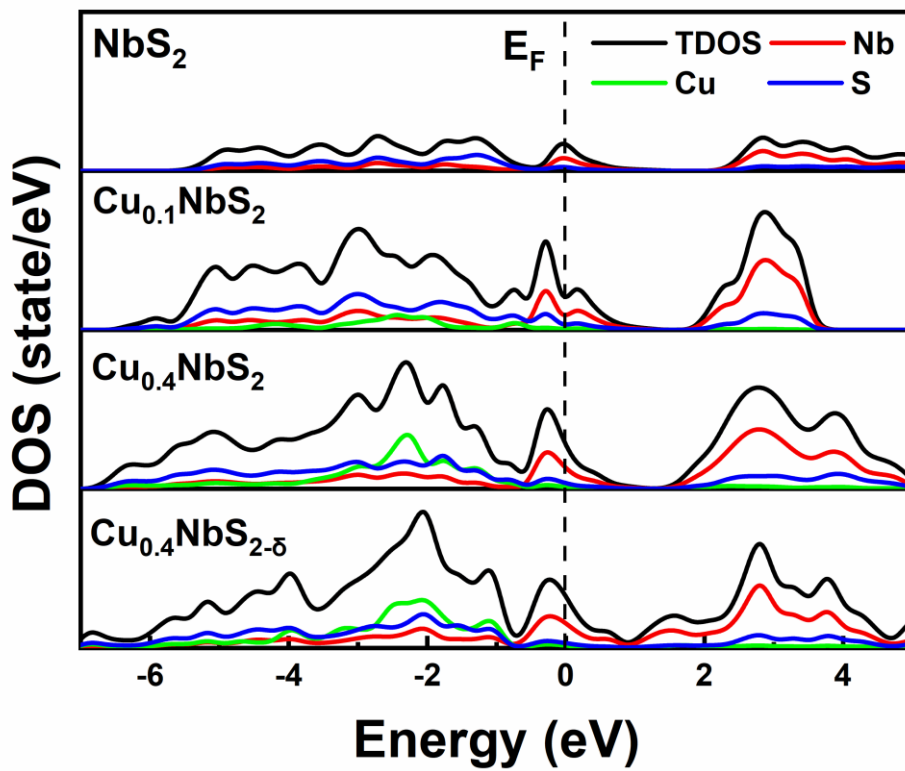


**Fig. S28** The density of states (DOS) of  $\text{NbS}_2$ ,  $\text{Cu}_{0.1}\text{NbS}_2$ ,  $\text{Cu}_{0.4}\text{NbS}_2$  and  $\text{Cu}_{0.4}\text{NbS}_{2-\delta}$ .

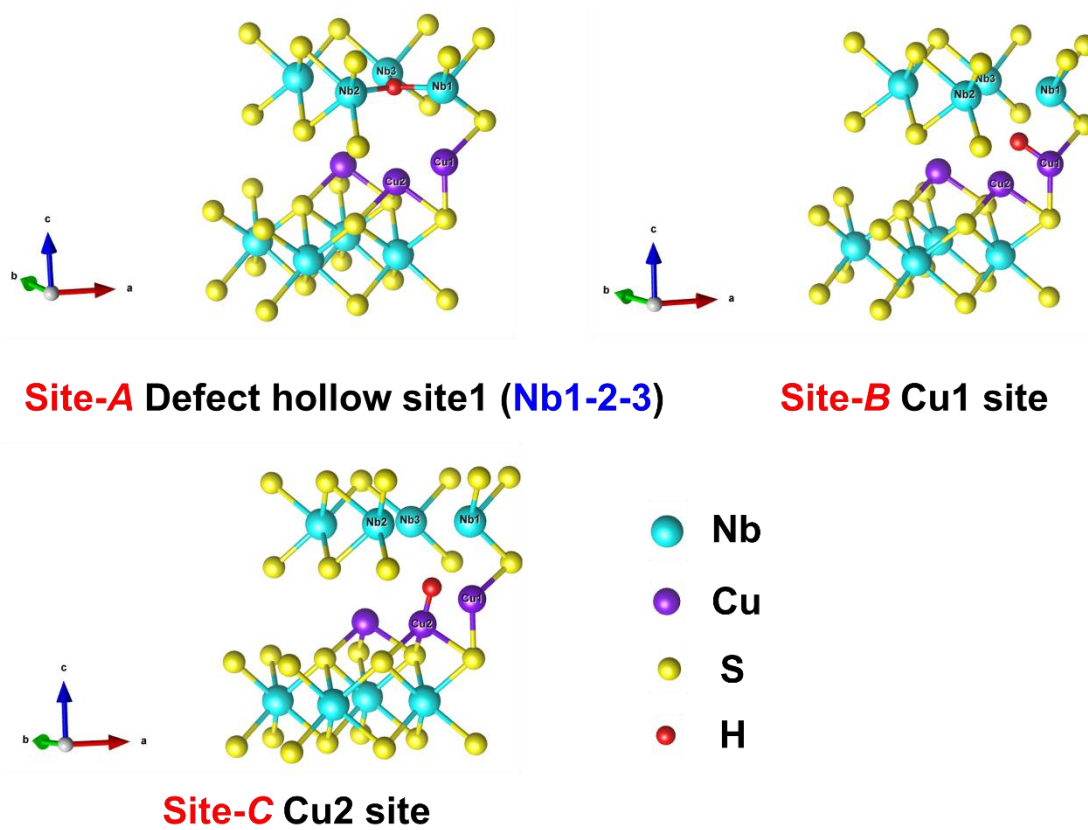


**Fig. S29** Schematic diagram of hydrogen spillover pathway 1 with different H adsorption sites in  $\text{Cu}_{0.4}\text{NbS}_{2-\delta}$ .

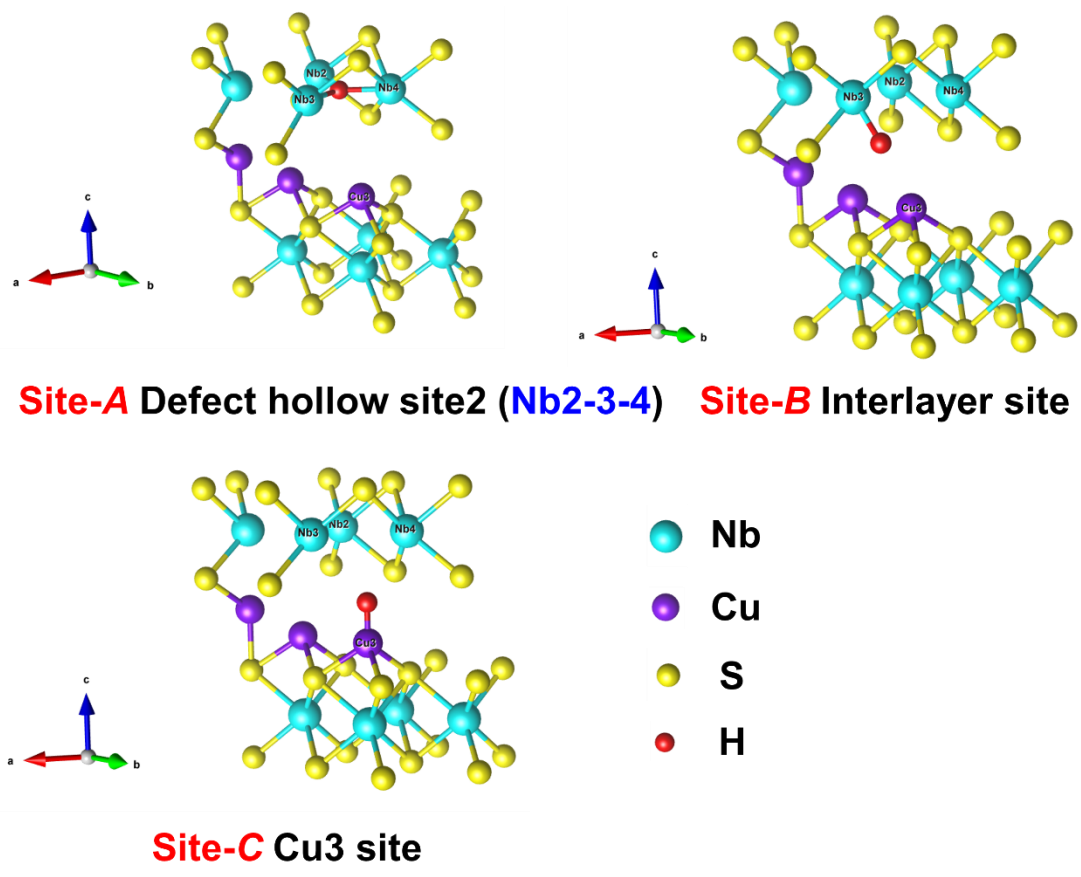


**Fig. S30** Schematic diagram of hydrogen spillover pathway 2 with different H adsorption sites in  $\text{Cu}_{0.4}\text{NbS}_{2-\delta}$ .

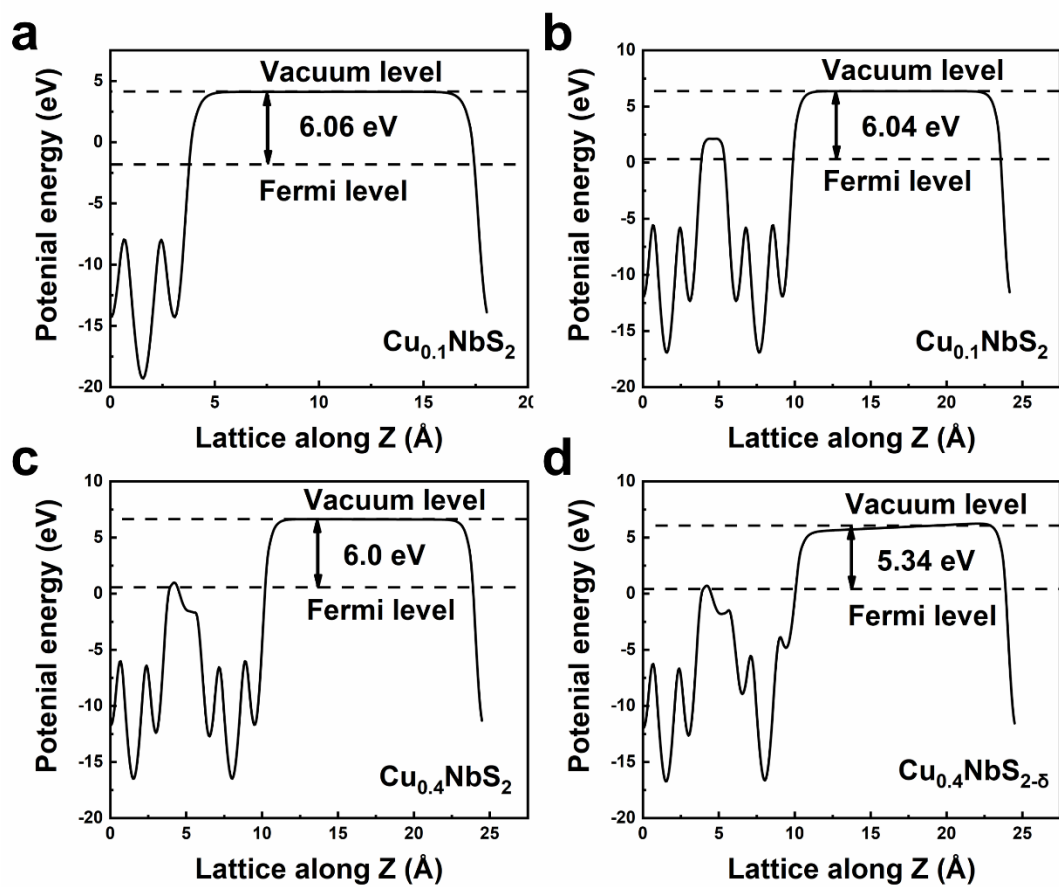


**Fig. S31** The calculated work functions ( $\Phi$ ) of (a)  $\text{NbS}_2$ , (b)  $\text{Cu}_{0.1}\text{NbS}_2$ , (c)  $\text{Cu}_{0.4}\text{NbS}_2$  and (d)  $\text{Cu}_{0.4}\text{NbS}_{2-\delta}$ .

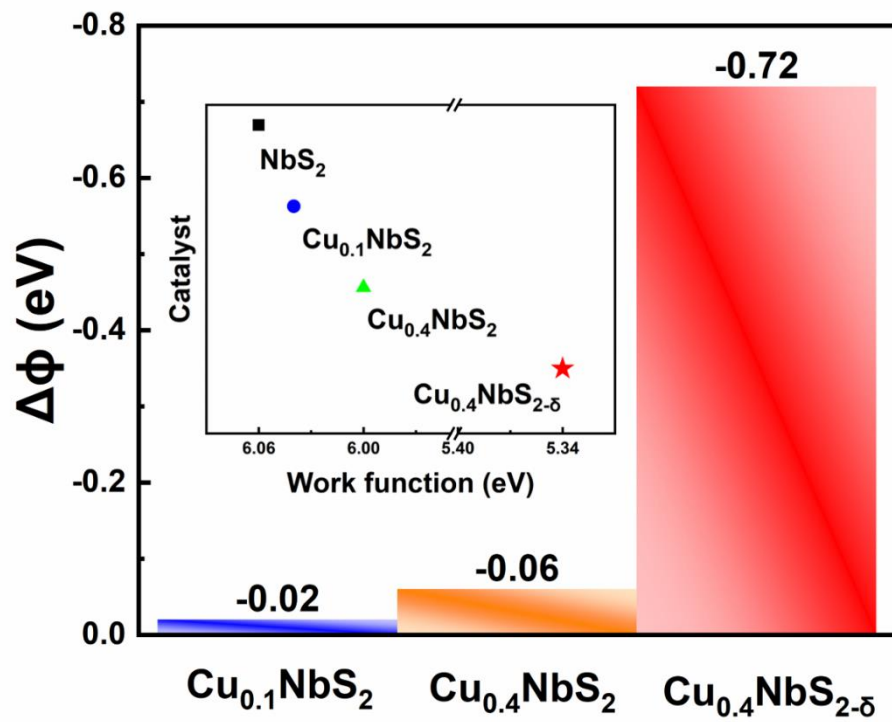


**Fig. S32** The differences of work function ( $\Delta\Phi$ ) between the three intercalated phases ( $\text{Cu}_{0.1}\text{NbS}_2$ ,  $\text{Cu}_{0.4}\text{NbS}_2$ ,  $\text{Cu}_{0.4}\text{NbS}_{2-\delta}$ ) and  $\text{NbS}_2$ . The calculated work functions are also shown inset.

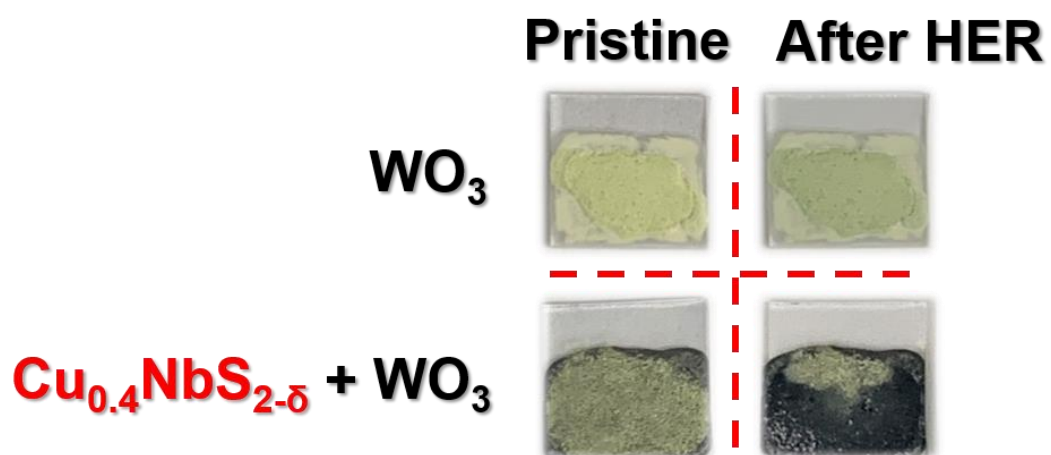


**Fig. S33** The photographs of the catalyst and  $\text{WO}_3$  mixtures showing the change in color. The upper part is pristine  $\text{WO}_3$  coating before and after HER on indium tin oxide (ITO) electrode. The lower part is pristine mixture coating and mixture coating after HER on ITO electrode.

**Table S1** The lattice parameters of  $\text{Cu}_{0.1}\text{NbS}_2$  and  $\text{Cu}_{0.4}\text{NbS}_2$  from Rietveld refinements.

<b>Sample</b>	$\text{Cu}_{0.1}\text{NbS}_2$	$\text{Cu}_{0.4}\text{NbS}_2$
<b>Space Group</b>	<i>P6<sub>3</sub>/mmc</i> (No. 194)	<i>P6<sub>3</sub>/mmc</i> (No. 194)
<b>a (Å)</b>	3.3278	3.3460
<b>b (Å)</b>	3.3278	3.3460
<b>c (Å)</b>	12.0511	13.0601
<b><math>\alpha</math> (°)</b>	90	90
<b><math>\beta</math> (°)</b>	90	90
<b><math>\gamma</math> (°)</b>	120	120
<b>Volume (Å<sup>3</sup>)</b>	115.57848	126.62550

**Table S2** Normalized atomic ratios in Cu<sub>0.4</sub>NbS<sub>2-δ</sub> as determined by XPS.

Sample	S/Nb ratio	Cu/Nb ratio
Cu <sub>0.4</sub> NbS <sub>2-δ</sub> -1	1.86	0.43
Cu <sub>0.4</sub> NbS <sub>2-δ</sub> -2	1.83	0.46
Cu <sub>0.4</sub> NbS <sub>2-δ</sub> -3	1.78	0.48

**Table S3** Comparison of HER activity for Cu<sub>0.4</sub>NbS<sub>2-δ</sub> with other reported NbS<sub>2</sub>-based electrocatalysts.

Sample	$\eta_{10}$ (mV)	Tafel (mV dec <sup>-1</sup> )	Electrolyte	Ref.
<b>Cu<sub>0.4</sub>NbS<sub>2-δ</sub></b>	<b>153</b>	<b>114.55</b>	<b>0.5M H<sub>2</sub>SO<sub>4</sub></b>	<b>This work</b>
<b>P-Se-NbS<sub>2</sub></b>	363	116.7	0.5M H <sub>2</sub> SO <sub>4</sub>	3
<b>Electrochemical exfoliated NbS<sub>2</sub></b>	236	125	0.5M H <sub>2</sub> SO <sub>4</sub>	4
<b>Li-TFSI-treated NbS<sub>2</sub></b>	310	-	0.5M H <sub>2</sub> SO <sub>4</sub>	5
<b>MoS<sub>x</sub>@NbS<sub>2</sub></b>	164	43.2	0.5M H <sub>2</sub> SO <sub>4</sub>	6
<b>NbS<sub>2</sub>/rGO</b>	500	72	0.5M H <sub>2</sub> SO <sub>4</sub>	7
<b>H-NbS<sub>2</sub></b>	50	30	0.5M H <sub>2</sub> SO <sub>4</sub>	8
<b>NbS<sub>2</sub></b>	900	133	0.5M H <sub>2</sub> SO <sub>4</sub>	9
<b>NbS<sub>2</sub>/Si Nanowire Heterojunction</b>	140	30	0.5M HClO <sub>4</sub>	10
<b>Pd<sub>0.23</sub>NbS<sub>2</sub></b>	157	50	0.5M H <sub>2</sub> SO <sub>4</sub>	11
<b>NbS<sub>2</sub>-Ppy-1</b>	210	54	0.5M H <sub>2</sub> SO <sub>4</sub>	12
<b>Mechanically exfoliated NbS<sub>2</sub></b>	188	99	0.5M H <sub>2</sub> SO <sub>4</sub>	13

**Table S4** The  $\Delta G_H^*$  of different sites in  $\text{Cu}_{0.4}\text{NbS}_2$ .

<b>Site</b>	<b><math>\Delta G_H^*</math> (eV)</b>
<b>S<sub>basal plane</sub></b>	0.455
<b>Cu1</b>	2.299
<b>Cu2</b>	2.191
<b>Interlayer</b>	2.547

## References

1. G. Kresse and J. Furthmüller, Efficient iterative schemes for ab initio total-energy calculations using a plane-wave basis set, *Phys. Rev. B*, 1996, **54**, 11169-11186.
2. J. P. Perdew, K. Burke and M. Ernzerhof, Generalized Gradient Approximation Made Simple, *Phys. Rev. Lett.*, 1996, **77**, 3865-3868.
3. W. Shen, L. Qiao, J. Ding and Y. Sui, P and Se-codopants triggered basal plane active sites in NbS<sub>2</sub> 3D nanosheets toward electrocatalytic hydrogen evolution, *Appl. Surf. Sci.*, 2022, **581**, 152419.
4. J. Si, Q. Zheng, H. Chen, C. Lei, Y. Suo, B. Yang, Z. Zhang, Z. Li, L. Lei, Y. Hou and K. K. Ostrikov, Scalable Production of Few-Layer Niobium Disulfide Nanosheets via Electrochemical Exfoliation for Energy-Efficient Hydrogen Evolution Reaction, *ACS Appl. Mater. Interfaces*, 2019, **11**, 13205-13213.
5. L. Najafi, S. Bellani, R. Oropesa-Nunez, B. Martin-Garcia, M. Prato, V. Mazanek, D. Debellis, S. Lauciello, R. Brescia, Z. Sofer and F. Bonaccorso, Niobium disulphide (NbS<sub>2</sub>)-based (heterogeneous) electrocatalysts for an efficient hydrogen evolution reaction, *J. Mater. Chem. A*, 2019, **7**, 25593-25608.
6. X. F. Zhou, S. H. Lin, X. L. Yang, H. N. Li, M. N. Hedhili, L. J. Li, W. J. Zhang and Y. M. Shi, MoS<sub>x</sub>-coated NbS<sub>2</sub> nanoflakes grown on glass carbon: an advanced electrocatalyst for the hydrogen evolution reaction, *Nanoscale*, 2018, **10**, 3444-3450.
7. D. Gopalakrishnan, A. Lee, N. K. Thangavel and L. M. R. Arava, Facile synthesis of electrocatalytically active NbS<sub>2</sub> nanoflakes for an enhanced hydrogen evolution reaction (HER), *Sustain. Energ. Fuels*, 2018, **2**, 96-102.
8. Y. Y. Liu, J. J. Wu, K. P. Hackenberg, J. Zhang, Y. M. Wang, Y. C. Yang, K. Keyshar, J. Gu, T. Ogitsu, R. Vajtai, J. Lou, P. M. Ajayan, B. C. Wood and B. I. Yakobson, Self-optimizing, highly surface-active layered metal dichalcogenide catalysts for hydrogen evolution, *Nat. Energy*, 2017, **2**, 17127.

9. X. Y. Chia, A. Ambrosi, P. Lazar, Z. Sofer and M. Pumera, Electrocatalysis of layered Group 5 metallic transition metal dichalcogenides ( $\text{MX}_2$ ,  $\text{M} = \text{V}, \text{Nb}, \text{and Ta}$ ;  $\text{X} = \text{S}, \text{Se}, \text{and Te}$ ), *J. Mater. Chem. A*, 2016, **4**, 14241-14253.
10. P. Gnanasekar, D. Periyanaounder, P. Varadhan, J. H. He and J. Kulandaivel, Highly Efficient and Stable Photoelectrochemical Hydrogen Evolution with 2D-NbS<sub>2</sub>/Si Nanowire Heterojunction, *ACS Appl. Mater. Interfaces*, 2019, **11**, 44179-44185.
11. C. Huang, X. Wang, D. Wang, W. Zhao, K. Bu, J. Xu, X. Huang, Q. Bi, J. Huang and F. Huang, Atomic Pillar Effect in Pd<sub>x</sub>NbS<sub>2</sub> To Boost Basal Plane Activity for Stable Hydrogen Evolution, *Chem. Mater.*, 2019, **31**, 4726-4731.
12. X. Gong, D. Kong, M. E. Pam, L. Guo, S. Fan, S. Huang, Y. Wang, Y. Gao, Y. Shi and H. Y. Yang, Polypyrrole coated niobium disulfide nanowires as high performance electrocatalysts for hydrogen evolution reaction, *Nanotechnology*, 2019, **30**, 405601.
13. J. Zhang, J. Wu, X. Zou, K. Hackenberg, W. Zhou, W. Chen, J. Yuan, K. Keyshar, G. Gupta, A. Mohite, P. M. Ajayan and J. Lou, Discovering superior basal plane active two-dimensional catalysts for hydrogen evolution, *Mater. Today*, 2019, **25**, 28-34.